Research Square

Preprints are preliminary reports that have not undergone peer review.
They should not be considered conclusive, used to inform clinical practice,
or referenced by the media as validated information.

Co-seismic Deformation and Structural Controls of the 3 August 2026 Mw 5.6 Suez Earthquake, Egypt, from Sentinel-1 InSAR, Seismicity and Satellite Gravity

Mahmoud S. Etman

mahmoud.etman@nriag.sci.eg

National Research Institute of Astronomy and Geophysics

Moataz Sayed

National Research Institute of Astronomy and Geophysics

Hussein. S. Abdullah

National Research Institute of Astronomy and Geophysics

Gad Qady

National Research Institute of Astronomy and Geophysics

Ahmed Hamed

National Research Institute of Astronomy and Geophysics

Mohamed S. Mahrous

National Research Institute of Astronomy and Geophysics

Article

Keywords: Gulf of Suez, Sentinel-1 InSAR, Seismicity, co-seismic deformation, fault geometry, satellite gravity

Posted Date: November 6th, 2026

DOI: https://doi.org/10.21203/rs.3.rs-11341362/v1

License: This work is licensed under a Creative Commons Attribution 4.0 International License.
Read Full License

Additional Declarations: No competing interests reported.

Co-seismic Deformation and Structural Controls of the 3 August 2026 Mw 5.6 Suez Earthquake, Egypt, from Sentinel-1 InSAR, Seismicity and Satellite Gravity

Mahmoud S. Etman[1*], Moataz Sayed[1], Hussein. S. Abdullah[1], Gad Qady[1], Ahmed Hamed[1] and Mohamed S. Mahrous[1]

[1] National Research Institute of Astronomy and Geophysics, Helwan, Egypt;

M.E.:mahmoud.etman@nriag.sci.eg, M.I.:moataz.ibrahim@nriag.sci.eg, H.A.:hussein.sabry@nriag.sci.eg,

G.Q.:gadosan@nriag.sci.eg, A.H.: ahmadhamed4@nriag.sci.eg, M.M.: mohamed.mahrous@nriag.sci.eg

[*]**Correspondence**: M.E.: mahmoud.etman@nriag.sci.eg

Abstract

One of the greatest instrumentally recorded occurrences in the Cairo-Suez area was the Mw 5.6 earthquake on August 3, 2026, which occurred north of Suez near the northern end of the Suez Rift. We investigate its surface deformation and structural setting by integrating Sentinel-1 interferometric synthetic aperture radar (InSAR), seismicity, focal-mechanism information and satellite-only gravity data. Co-seismic interferograms from ascending Track 160 (22 July–3 August 2026) and descending Track 94 (24 July–5 August 2026) were processed with GMTSAR, supplemented by ascending Track 58 and a pre-event LiCSAR interferogram (frame 094D_05947_131210). The processed fields show maximum line-of-sight (LOS) displacements of ~4 cm (ascending) and ~3 cm (descending) around the epicentral area, superimposed on long-wavelength components; the fault-localized LOS step across the nearest mapped fault is ~7 mm. Decomposition of the two geometries yields E–W and vertical components of up to ~2.5 cm and ~3.05 cm, respectively. A pre-event interferogram shows only a weak, spatially limited anomaly that cannot be regarded as precursory. Seismicity and the focal-mechanism solution indicate predominantly normal faulting on a NW–SE-striking plane (strike ~326°, and 152°, dips of 35° and 55°) in the integrated model). Gravity data reveal a density boundary near the epicenter, with SI = 1 Euler solutions yielding a median depth of 14.8 km and a dominant NNW–SSE trend (338°/158°). These findings agree with the regional rift orientation and the InSAR-derived fault depth of 17.6 km. The spatial agreement between deformation, seismicity and gravity-derived structures suggests that the earthquake ruptured a pre-existing rift-related structure, providing new constraints on active deformation and seismic hazard in the northern Suez Rift.

Keywords: Gulf of Suez; Sentinel-1 InSAR; Seismicity; co-seismic deformation; fault geometry; satellite gravity

1. Introduction

Earthquake-related crustal deformation provides important constraints on the accumulation and release of tectonic strain and on the geometry and kinematics of active faults. The combination of radar interferometric readings with seismicity and subsurface structure data might therefore aid in the assessment of earthquake causes and tectonic controls. An efficient method for mapping ground deformation caused by earthquakes across wide areas with high spatial

resolution is Interferometric Synthetic Aperture Radar (InSAR). Repeat-pass SAR observations can detect millimeter- to centimeter-scale changes in the radar line-of-sight (LOS), while combining ascending and descending geometries provides complementary constraints on the deformation field (Hanssen, 2001; Bürgmann et al., 2006; Hooper et al., 2012; Merryman Boncori, 2019). The availability of Sentinel-1 observations has further expanded the application of InSAR to earthquake and tectonic studies, while processing and time-series packages, such as GMTSAR and LiCSBAS, respectively, facilitate the generation and analysis of interferometric deformation products (Sandwell et al., 2011; Morishita et al., 2020).

The Gulf of Suez is a large continental rift system in northeastern Egypt that serves as the northern continuation of the Red Sea extensional system. Its NW–SE-trending structural framework includes major normal faults, tilted fault blocks, half-grabens, and inherited basement-controlled structures formed mainly during Oligocene–Miocene extension. Although the principal rifting phase declined during the Miocene, geological, geomorphological, seismic, and geodetic observations indicate that deformation has continued during the Quaternary and Recent periods (Bosworth & Taviani, 1996; Riguzzi et al., 2006; Bosworth et al., 2019; Fernandez-Blanco et al., 2025). Recent geomorphic evidence indicates continued normal faulting and low-rate extension, with estimated Pleistocene–Recent extension rates of approximately 0.26–0.55 mm/yr. (Fernandez-Blanco et al., 2025). Seismic activity serves as another sign of current deformation occurring in the rift.

Both historical and recent earthquakes, along with focal-mechanism analyses, typically show normal to oblique-normal faulting, which represents the intricate extensional and transtensional deformation of the area (Hussein et al., 2006; Abdelazim et al., 2016; Bosworth et al., 2019). Gravity observations provide an independent constraint on the subsurface framework by revealing variations in basement depth, crustal density, and buried structural boundaries, and can therefore help relate observed deformation and seismicity to major fault systems (Sayed et al., 2025; Farag et al., 2022). Geodetic and InSAR observations in Wadi Hagul have revealed measurable ground deformation, providing regional context for assessing tectonic activity in the Gulf of Suez (Etman et al., 2025).

On 3 August 2026, an Mw 5.6 earthquake occurred in the Suez region at a reported focal depth of approximately 10 km. Its location within the Suez Rift provides a recent opportunity to examine the relationship between moderate seismicity, surface deformation, and the established tectonic framework. Accordingly, this study investigates the pre- and co-seismic deformation associated with the Suez earthquake using Sentinel-1 InSAR, seismicity, focal-mechanism information, and gravity anomalies to explore the deformation linked to earthquakes, characteristics of seismic sources, the geometry of causative faults, and adjacent subsurface formations. It also examines possible pre-earthquake deformation and assesses the event within the inherited rift-related tectonic framework. The study area and its structural setting are presented in (Fig. 1).

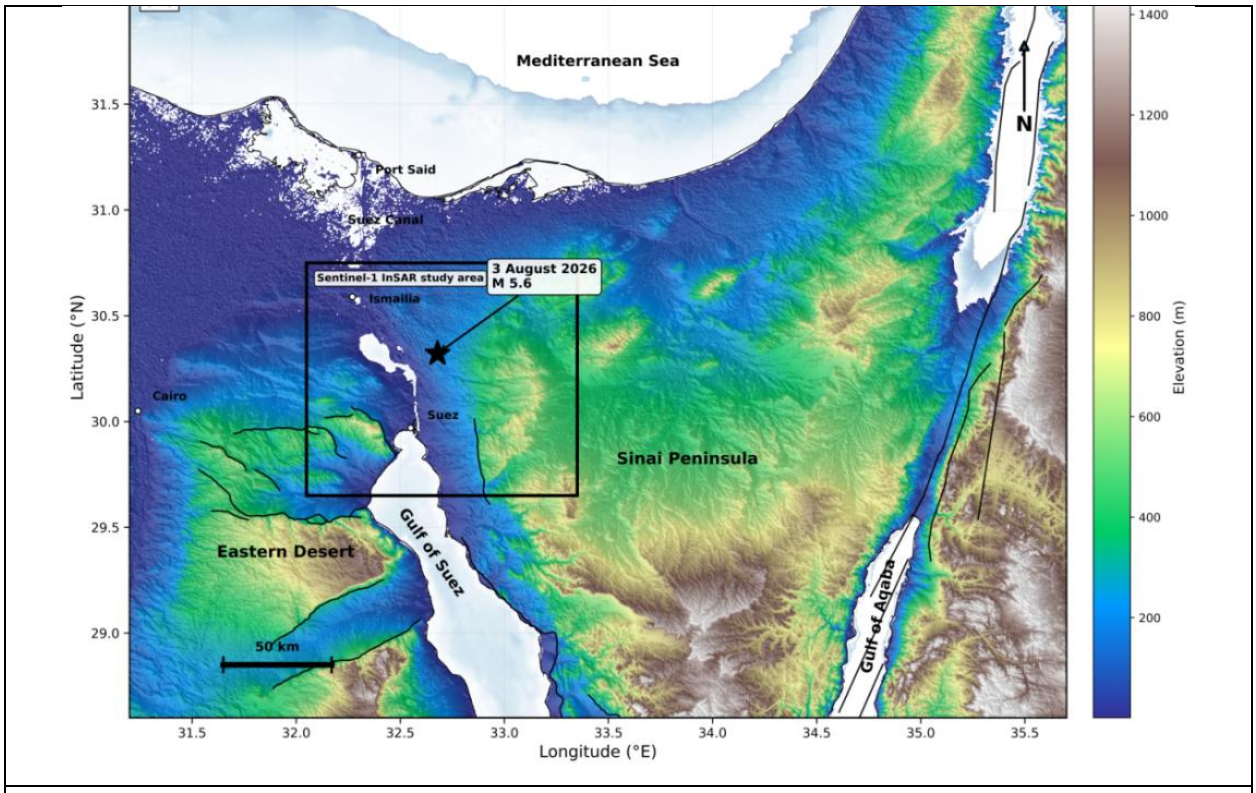


Fig.1: Location and structural setting of the study area at the northern termination of the Suez Rift, showing the epicenter of the 3 August 2026 Mw 5.6 Suez earthquake. Base data: SRTM 30 m; GEM Global Active Faults Database (Styron & Pagani, 2020).

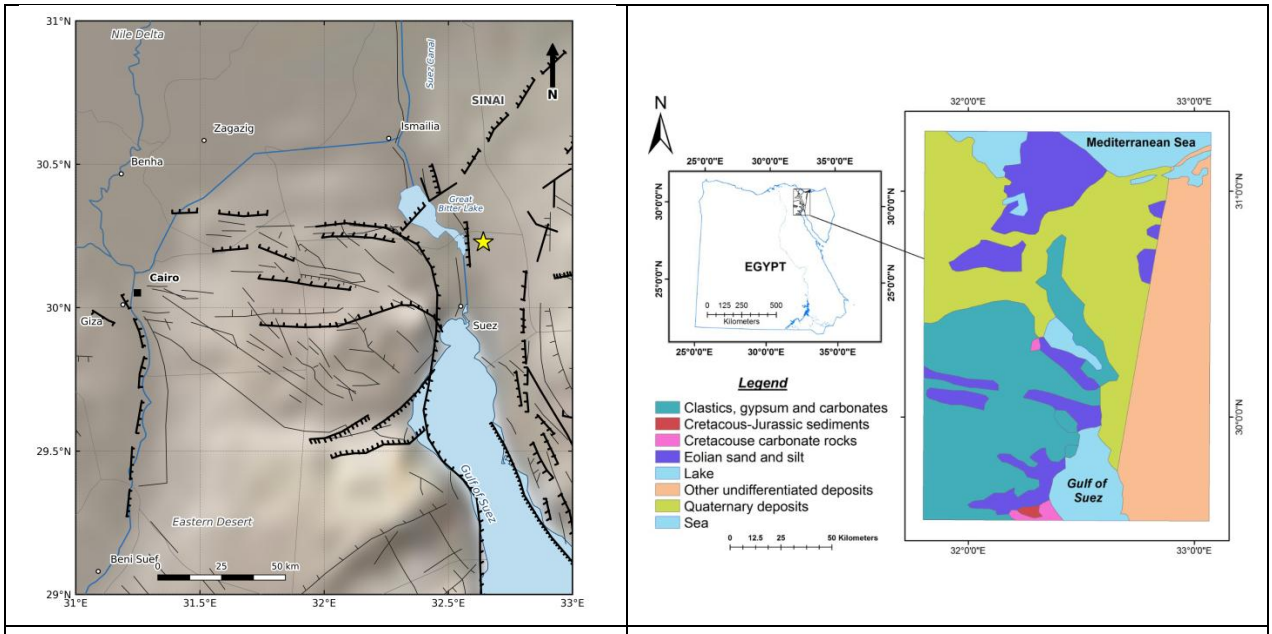
2. Geological Setting and Seismicity

The study area lies in northern Egypt within the Gulf of Suez Rift, a major continental rift extending northwestward from the Red Sea and separating the African mainland from the Sinai structural domain. Its evolution reflects the relative motion of the African and Arabian plates and the development of the Sinai block. The rift is characterized by major normal faults, tilted fault blocks, structural highs, and sedimentary sub-basins, with its architecture strongly influenced by inherited basement structures and successive phases of extension.

The dominant structural trends are NW–SE to NNW–SSE, accompanied by subordinate cross-cutting structures (Colletta et al., 1988; Moustafa & Abd-Allah, 1992; Gawthorpe et al., 2003; Bosworth et al., 2005). The Gulf of Suez developed mainly during Oligocene–Miocene extension, with early extension rates estimated at ~2–4 mm/yr. (Steckler et al., 1988), before plate-boundary motion was progressively transferred eastward to the Gulf of Aqaba–Dead Sea transform system. Present-day geodetic measurements indicate slower extension across the Gulf of Suez (Mahmoud et al., 2005). According to Salamon et al. (2003) and Hussein et al. (2006, 2013), NW–SE to NNW–SSE high-angle normal faults mostly accommodate the regional stress field, which is typically ENE–WSW to NE–SW extensional.

The lithological framework consists of Precambrian basement rocks overlain by Paleozoic–Mesozoic pre-rift sediments and younger Cenozoic successions. The sedimentary cover comprises broadly defined pre-rift, syn-rift, and post-rift sequences, with Oligocene–Miocene deposits forming the principal syn-rift succession and Pliocene–Quaternary sediments constituting the younger cover (Alsharhan, 2003; Jackson et al., 2006). Their distribution and thickness are closely controlled by fault-related basin development and provide an important framework for interpreting the structural and deformation patterns observed in the study area (Gawthorpe et al., 2003; Jackson et al., 2006). The distribution and geometry of major faults, structural lineaments, main lithological units and their spatial distribution are shown in (Fig. 2).

The area continues to experience seismic activity, with earthquakes focused along significant rift formations and related fault lines. Previous focal-mechanism studies indicate predominantly normal to oblique-normal faulting, with local strike-slip components related to inherited structures and spatial variations in the stress field (Salamon et al., 2003; Hussein et al., 2006; Abdelazim et al., 2016). Hypocentres commonly occur at ~5–30 km depth (El Khrepy et al., 2016). The northern Gulf of Suez and the Cairo–Suez district form a structural transition where rift-related deformation interacts with inherited inland structures, including the Gebel Ataqa fault system (Moustafa & Abd-Allah, 1992). The regional distribution of earthquakes of magnitude 3.5 to >6 is shown in (Fig. 3).



a) **b)**

Fig.2: Geological framework of the study area, showing (a) the distribution and geometry of major faults and structural lineaments, and (b Lithological map of the study area in northern Egypt (bounded by the Mediterranean Sea and northern Gulf of Suez), mapped from U.S. Geological Survey (USGS) data.

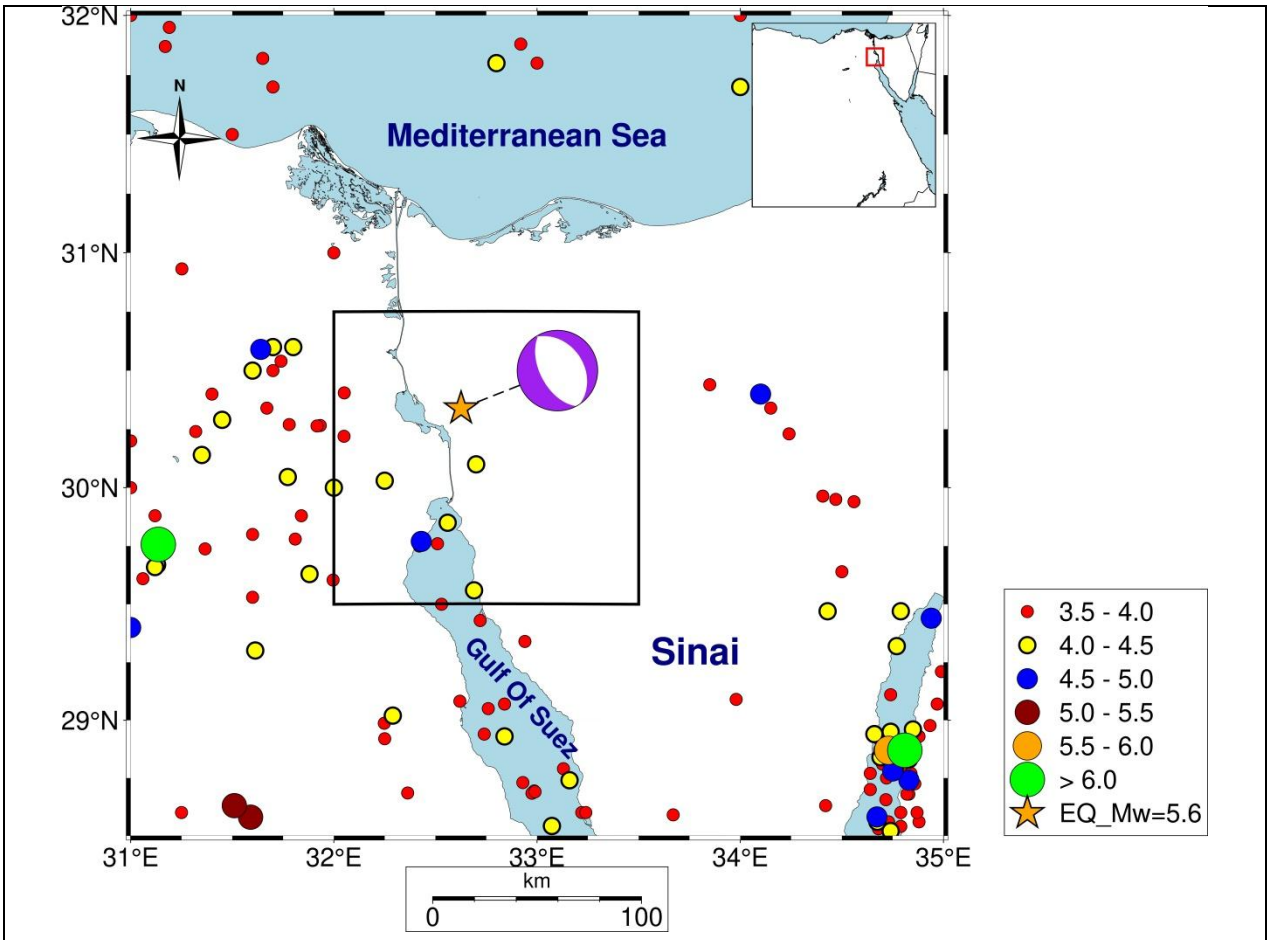


Fig.3: Seismicity map of study and the Sinai region showing earthquake events recorded by the Egyptian National Seismic Network (ENSN) from 1900 to 2026.

3. Methodology and Data Processing

3.1. Sentinel-1 SAR Data

Sentinel-1 data were obtained from the Alaska Satellite Facility (ASF) and the COMET LiCSAR system. Sentinel-1A SAR imagery has been widely used to derive interferometric deformation measurements, with seismicity data providing complementary information for interpreting observed ground movements (Etman et al., 2022). Three single-look complex (SLC) pairs were processed using GMTSAR: ascending Track 58 (27 July–8 August 2026), ascending Track 160 (22 July–3 August 2026), and descending Track 94 (24 July–5 August 2026). The earthquake occurred on 3 August 2026 at about 03:00 local time (00:00 UTC). The Track 160 and Track 94 pairs span the earthquake, with post-event acquisitions on 3 August (after 03:35 am local time) and 5 August, respectively, and provide the principal observations of the earthquake-related deformation. The Track 58 pair also spans the event but includes a longer post-seismic interval

(about five days). In addition, the LiCSAR interferogram for frame 094D_05947_131210 (24–30 July 2026), which shares the relative orbit of descending Track 94, was used to assess possible pre-earthquake deformation (Table 1). All data were acquired in Interferometric Wide Swath (IW) mode. The ascending observations were acquired in VV + VH polarization, with incidence angles of approximately 34.2°–44.1° and headings of −12.65° for Track 58 and −12.67° for Track 160. The acquisition geometries and spatial coverage are shown in (Fig. 4).

Table 1: Sentinel-1 SAR data and interferometric pairs used in this study

Frame	Direction	Platform	Dates	Interferometric Role	Temporal baseline	Polarization
58	Ascending	Sentinel-1C	27 Jul, 08 Aug 2026	Pre-/main shock temporal analysis	12 days	VV + VH
160	Ascending	Sentinel-1C	22 Jul, 03 Aug 2026	co-seismic pair	12 days	VV + VH
94	Descending	Sentinel-1C	24 Jul, 5 Aug 2026	Co-seismic pair	12 days	VV+VH
094D_05947_131210	Descending	Sentinel-1 LiCSAR	24 Jul, 30 Jul 2026	Independent viewing geometry	6 days	VV

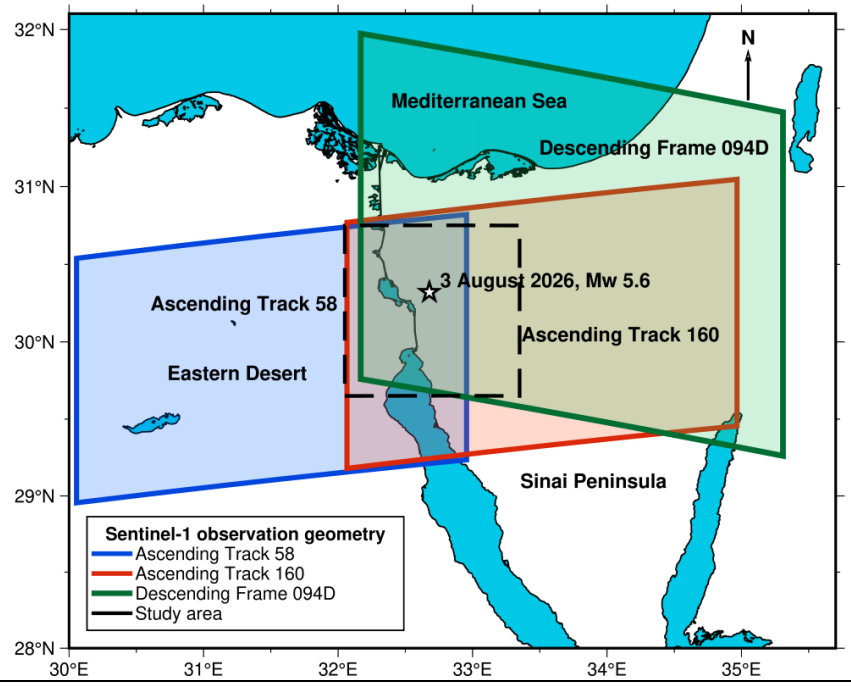


Fig.4: Sentinel-1 ascending and descending acquisition geometries and spatial coverage used in the InSAR analysis.

3.2 InSAR Processing

A two-pass differential InSAR (D-InSAR) strategy was adopted, with pairs selected to minimize temporal and geometric decorrelation while preserving the earthquake signal. Precise-orbit correction, TOPS co-registration, interferogram generation, topographic phase removal using the 1-arc-second (~30 m) SRTM DEM, Goldstein filtering, coherence estimation, phase unwrapping with SNAPHU, geocoding, and conversion to LOS displacement were among the processing methods used in GMTSAR (Sandwell et al., 2011) (Luo et al., 2021; Zhu et al., 2025).

A stable area outside the main deformation zone was used as the displacement reference. LiCSAR/LiCSBAS products were used to inspect the pre-event interval (Morishita et al., 2021). Ascending and descending LOS measurements were combined to estimate E–W and vertical displacements, neglecting the less-sensitive N–S component. Atmospheric delays, orbital residuals, DEM errors, and phase noise may affect the inferred deformation. Although GACOS was available, no atmospheric correction was applied; therefore, broad LOS patterns of 4–4.5 cm and the 6.7 mm fault-related step were interpreted cautiously, as these magnitudes may overlap with atmospheric and orbital uncertainties (Yu et al., 2018).The processing workflow is summarized in (Fig. 5).

Pre-event signals were assessed using their spatial coherence, persistence, consistency between independent observations and compatibility with the co-seismic pattern, and were classified as pre-event deformation rather than pre-seismic (precursory) deformation unless all these criteria were met (Guo et al., 2022; Zhu et al., 2025). The resulting deformation fields were compared with seismicity, the fault model and gravity-derived structures to evaluate their relationship to the structural framework of the Suez region.

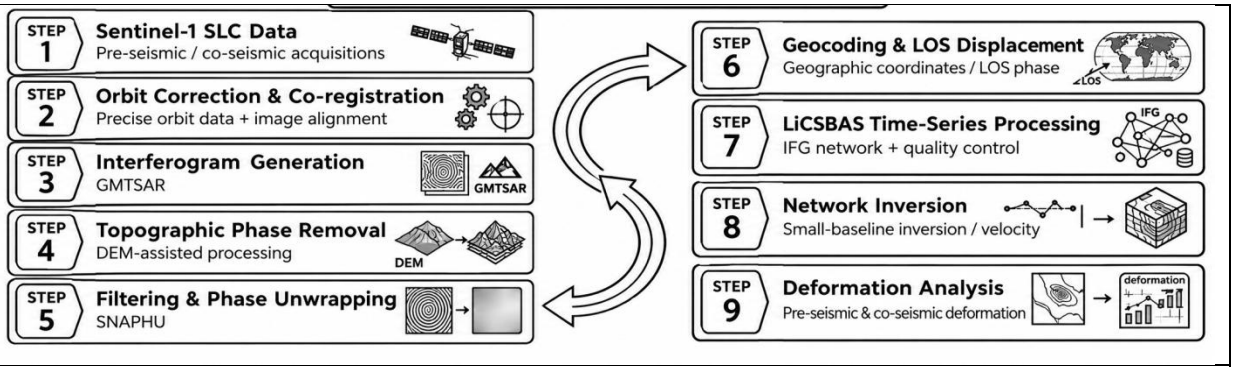


Fig.5: Processing workflow of Sentinel-1 D-InSAR data using GMTSAR and LiCSAR/LiCSBAS.

3.3 Gravity Data and Processing

Gravity data were derived from the satellite-only GOCO2025s global gravity model (Öhlinger et al., 2026), accessed through ICGEM (Ince et al., 2019), and referenced to GRS80 (Moritz, 1980). Normal gravity was removed to obtain the gravity disturbance, while topographic and bathymetric effects were calculated from the 1-arcminute ETOPO1 model using the tesseroid approach (Uieda et al., 2016), with a crustal density of 2.67 g cm^{-3} and a seawater–crust density contrast of −1.64 g cm^{-3} (Hinze, 2003). Gravity and magnetic investigations have been applied to characterize subsurface structures and basement geometry in the Wadi Hagul region, using anomaly filtering, Euler deconvolution, and 2D forward modeling to delineate major structural trends (Etman et al., 2025).

These corrections yielded the Bouguer anomaly. For structural analysis, the Bouguer grid was extended and cosine-tapered before frequency-domain processing. A regional Moho correction based on an integrated GOCE–seismic model (Sayed et al., 2025) was applied to obtain the residual gravity field. Euler deconvolution (SI = 0, 1, and 2) and structure-tensor analysis were then used to identify subsurface structures and their dominant orientations near the earthquake epicenter. An independent structural reference was supplied by active faults from the GEM Global Active Faults Database (Styron & Pagani, 2020). The earthquake epicenter (30.2278°N, 32.6411°E; depth 11.69 km), as reported by NRIAG, was compared with gravity anomalies and mapped structural boundaries to assess its relationship with the tectonic framework of the 3 August 2026 earthquake.

3.4 Seismicity and Focal Mechanism

The earthquake catalog, which spans the years 1900–2026, was acquired from the National Research Institute of Astronomy and Geophysics (NRIAG) via the Egyptian National Seismological Network (ENSN). Approximately 30 events occurring immediately before and after the 3 August 2026 main shock were selected for analysis, with magnitudes predominantly between ML 1.5 and 3.5. Epicenters are predominantly aligned with the regional structural trends of the Gulf of Suez, and hypocentral depths range from ~1 to ~27 km.

Most events are of low magnitude (M 1.5–2.5), with mean and median magnitudes of 2.36 and 2.32, respectively; the Mw 5.6 main shock is the largest event in the analyzed period. (Table 2) shows main shock and after shock in side table red color main shock and black color after shock. As seen in (Fig. 6) the temporal distribution shows relatively low background seismicity followed by a marked increase around 3 August 2026, corresponding to the main shock and subsequent activity (Fig. 6a, c). The magnitude–depth distribution (Fig. 6b) shows that most events are of low magnitude and occur in the upper ~20 km, with a few events reaching ~27 km.

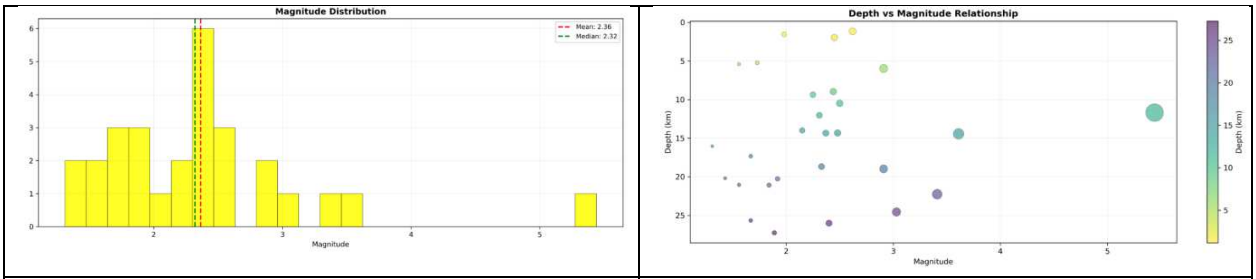
This episodic pattern is consistent with previously reported seismicity in the extensional Gulf of Suez region (Morsy et al., 2011; Hussein et al., 2013). Based on a lower-hemisphere

stereographic projection, (Fig. 7) depicts the focal mechanism of the earthquake that occurred in the northern Gulf of Suez on August 3, 2026. In line with the local extensional tectonic regime, the solution mostly shows pure normal faulting. The two nodal planes have strikes of 326° and 152°, dips of 35° and 55°, and rake angles of −95° and −87°, respectively. The principal stress axes further support this interpretation, with the P-axis oriented nearly vertically (plunge = 79°, azimuth = 74°) and the T-axis nearly horizontally (plunge = 10°, azimuth = 339°). First-motion polarity data show a good agreement with the calculated mechanism, with 16 consistent and only 1 inconsistent observation. Although there may still be some doubt because of station distribution and polarity identification, the focal mechanism generally offers compelling evidence for normal faulting linked to the Gulf of Suez's extensional tectonics.

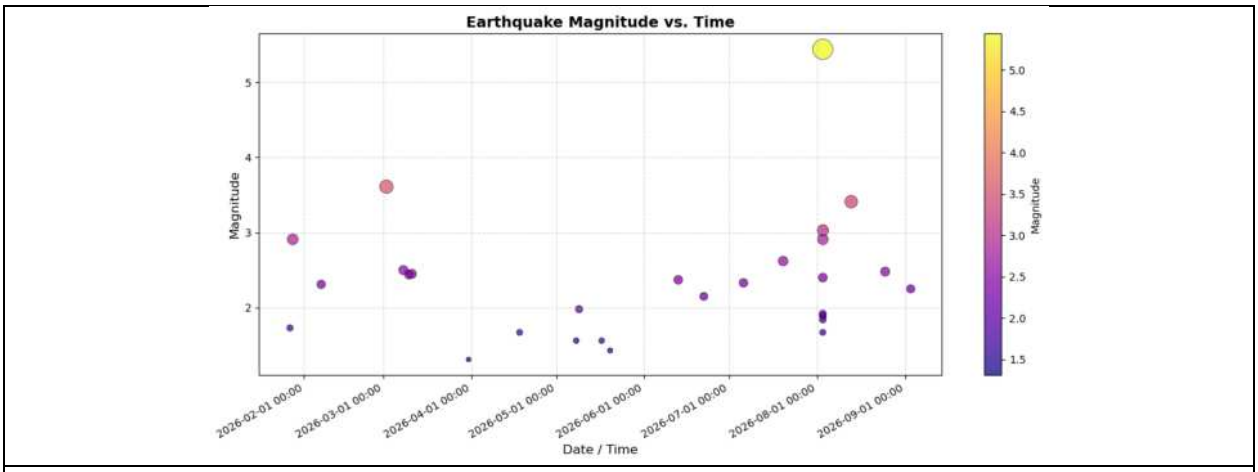
The co-seismic source was modeled as an elastic dislocation in a homogeneous half-space following Okada (1985). The fault plane comprised 24 sub-faults (6 × 4) spanning approximately 42 × 26 km, with a top depth of 4 km. Geometry was constrained by regional structures, focal mechanisms, and ascending–descending LOS observations. Model fit was assessed using RMS residuals for each viewing geometry and the combined dataset.

Table 2: Main shock and after shock in side red color main shock and black color after shock.

Date	Origin Time	Latitude	Longitude	Depth	magnitude
8/3/2026	00:35.7	30.2278	32.6411	11.69	5.44
8/3/2026	34:40.1	30.1833	32.5602	24.56	3.03
8/3/2026	49:55.2	30.2968	32.6143	26.01	2.4
8/3/2026	22:19.5	30.2119	32.5898	27.26	1.89
8/3/2026	37:39.4	30.275	32.6023	21.09	1.84
8/3/2026	36:23.5	30.2631	32.6187	20.26	1.92
8/3/2026	33:48.2	30.2323	32.6331	18.98	2.91
8/3/2026	17:14.3	30.2596	32.6024	17.33	1.67
8/13/2026	49:10.6	30.227	32.6075	22.26	3.41
8/25/2026	41:12.2	30.2153	32.6706	14.33	2.48
9/3/2026	31:54.9	30.2372	32.6436	9.37	2.25

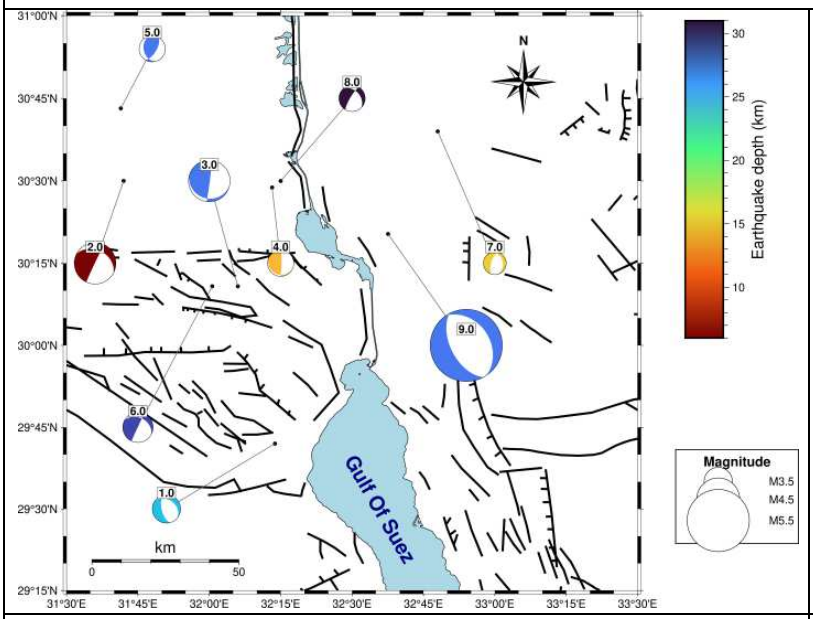


(a) **(b)**

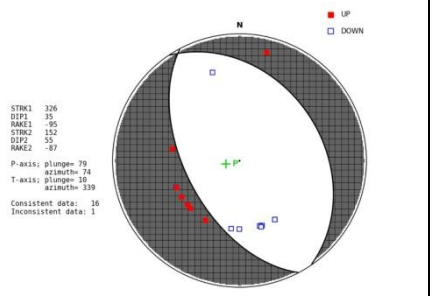


(c)

Fig.6: Seismicity characteristics of the study area: (a) earthquake magnitude distribution, (b) hypo central depth versus magnitude, and (c) monthly earthquake-event counts showing the temporal variation in background seismicity and the August 2026 earthquake sequence.



(a)



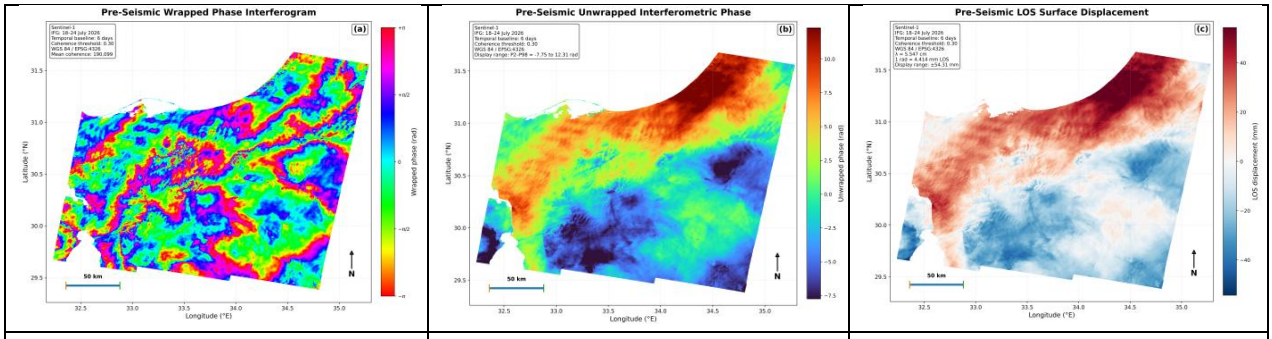
(b)

Fig.7: a) Seismotectonic map of the Gulf of Suez region depicting fault traces alongside focal mechanism solutions for the main shock and surrounding preshocks; b) Focal mechanism for the main earthquake. This data acquired from ENSN/ NRIAG.

4. Results

4.1 Pre-event Deformation

A LiCSBAS time-series analysis was performed using Sentinel-1 acquisitions at 6-day intervals from May to July 2026, with a mean interferometric coherence of approximately 0.6. Displacements were measured relative to a stable reference area (Fig. 8). The epicentral time series exhibited weak fluctuations without a sustained trend before the 3 August 2026 earthquake. An independent LiCSAR interferogram spanning 24–30 July 2026 was also examined for localized deformation. However, the weak signal could not be confidently distinguished from atmospheric and residual interferometric noise. Accordingly, the available observations provide no clear evidence of detectable pre-event deformation, although signals below the method's detection threshold cannot be excluded.

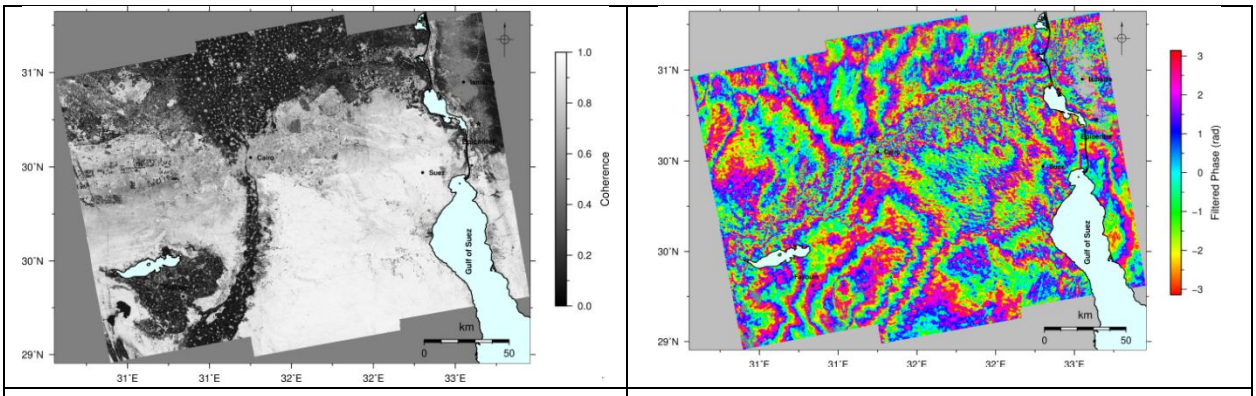


(a)	(b)	(c)

Fig.8: Pre-seismic descending LiCSBAS observations: (a) filtered interferometric phase, (b) unwrapped phase, and (c) LOS displacement.

4.2 Coherence and interferometric phase

The coherence map of the Track 58 pair (27 July–8 August 2026) shows generally high coherence across the desert areas, with reduced coherence over the cultivated Nile Delta and Valley, water bodies, and localized zones of decorrelation (Fig. 9a). The coherence information was used to identify reliable areas for phase interpretation and to exclude strongly decorrelated pixels. The filtered interferometric phase (Fig. 9b) displays spatially variable patterns across the track, including broad, long-wavelength phase variations extending well beyond the epicentral area, particularly toward Fayoum and Beni Suef. Given their large distance from the earthquake source, these signals are not interpreted as earthquake-related tectonic deformation and are instead attributed to non-tectonic effects, most likely atmospheric phase delays and residual orbital or long-wavelength interferometric artifacts. Accordingly, the interpretation of earthquake-related deformation is restricted to the coherent phase signals spatially associated with the epicentral region.

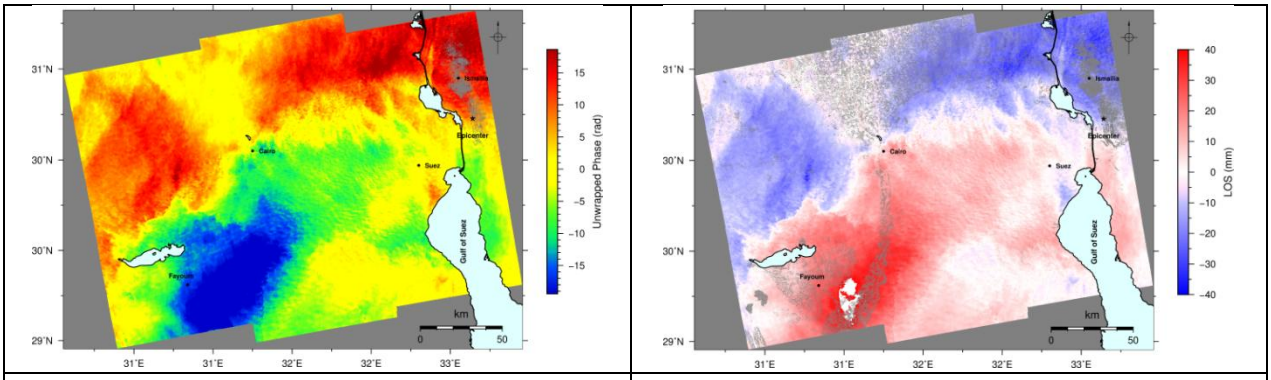


(a) **(b)**

Fig.9: Sentinel-1C ascending Track 58 interferometric results for the 27 July–8 August 2026 acquisition pair: (a) coherence mask and (b) filtered interferometric phase.

4.3 Co-seismic deformation

The LOS displacement map shows a broad deformation field, with positive values dominating parts of the southern and south-western scene and negative values occurring mainly across the northern and north-western areas (Fig. 10). The spatial extent of these patterns, including areas far from the Suez earthquake epicenter, indicates that the observed signal should be interpreted cautiously. Although the map provides a regional view of LOS displacement, the broad spatial variations cannot be attributed exclusively to earthquake-related deformation without further assessment of atmospheric and orbital contributions. The interpretation therefore focuses on the displacement pattern near the epicentral region and its relationship to the mapped structures (Fig. 11). However, the map alone does not establish that the observed deformation is localized on the causative fault. In particular, the reported 6.7 mm displacement step across the nearest mapped fault requires an uncertainty estimate and comparison with the source-model prediction before it can be interpreted as a tectonic signal. The distinction between the broad regional displacement field and the smaller local displacement change is essential for evaluating the reliability of the inferred co-seismic deformation.



(a) **(b)**

Fig.10: Sentinel-1 ascending Track 160 co-seismic deformation for the 22 July–3 August 2026 pair: (a) unwrapped phase and (b) LOS displacement.

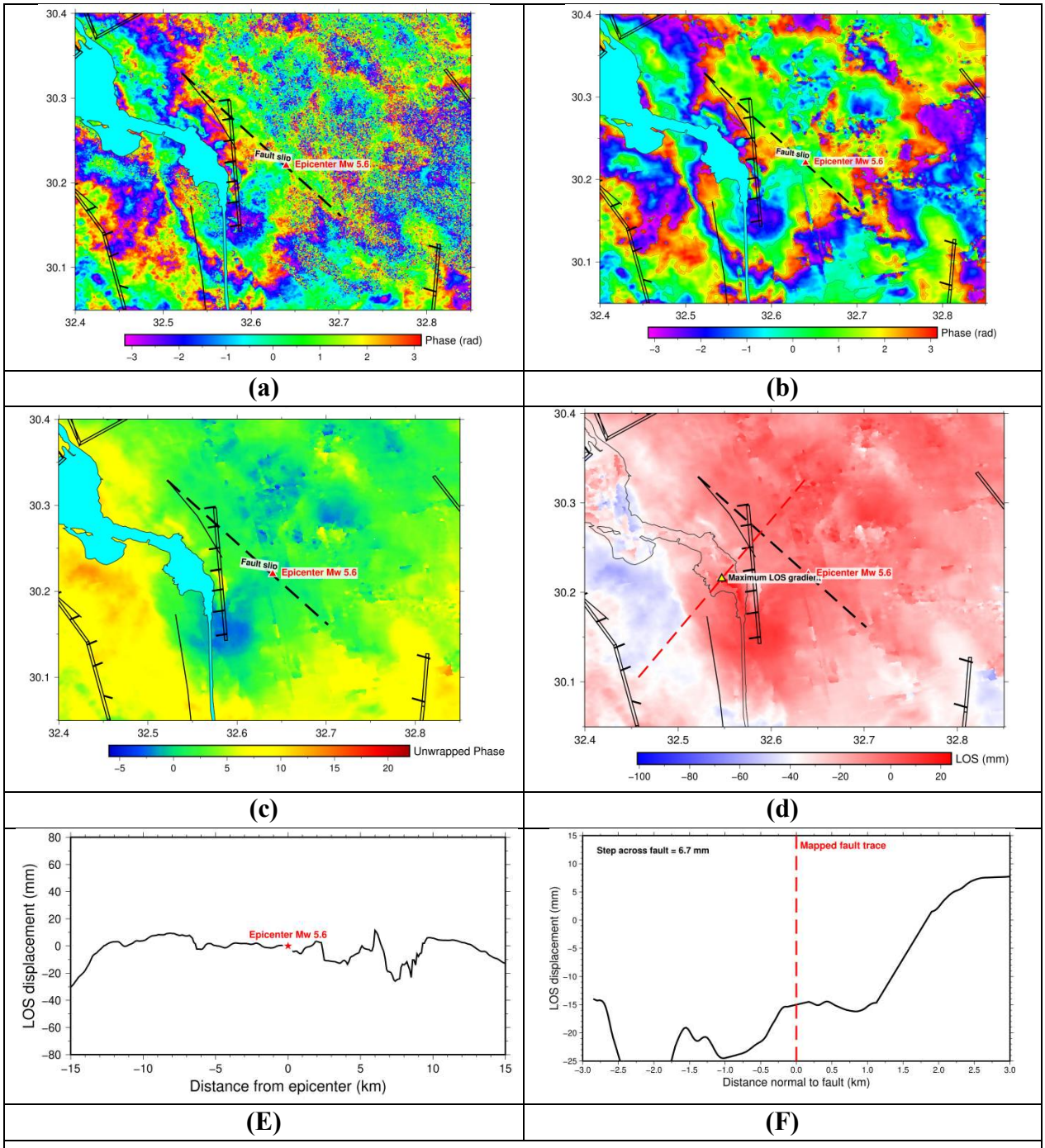


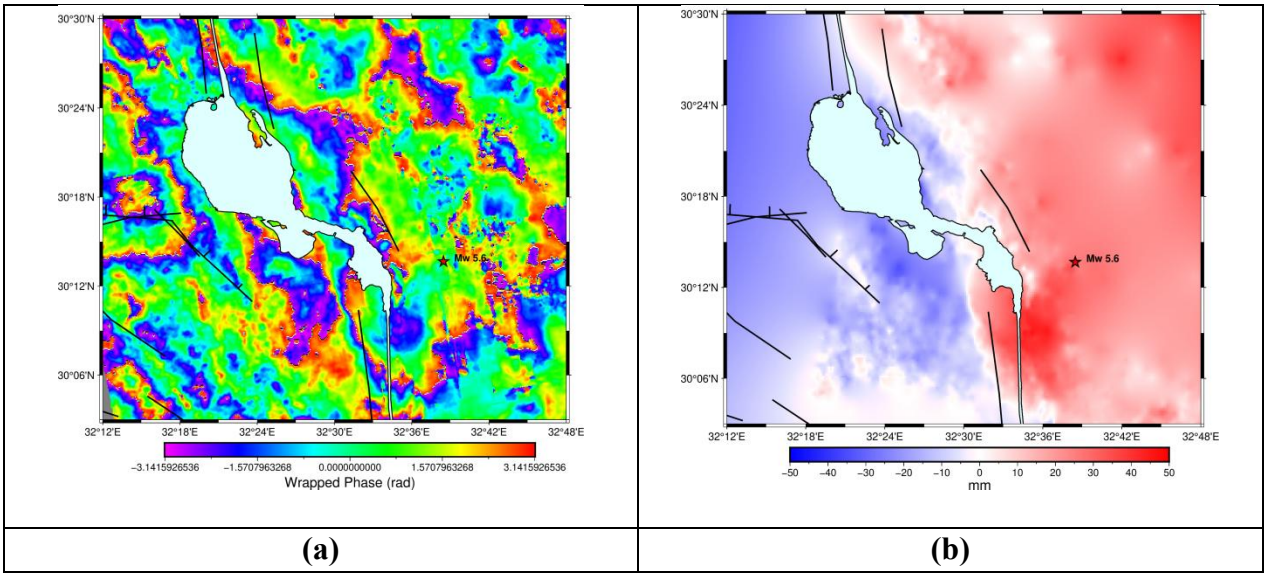
Fig.11: Co-seismic deformation analysis of the Sentinel-1C ascending Track 160 pair (22 July–3 August 2026): (a) interferometric phase, (b) filtered phase, (c) unwrapped phase, (d) LOS gradient profile, (e) LOS profile across the epicenter, and (f) LOS profile across the nearest mapped fault.

4.4 Ascending–descending comparison

The ascending and descending Sentinel-1 observations provide complementary viewing geometries for characterizing the co-seismic deformation field. The analysis integrates the 22 July–3 August 2026 ascending Track 160 pair with the 24 July–5 August 2026 descending Track 94 pair (Fig. 12). Both geometries show coherent deformation around the earthquake epicentral area, although the LOS amplitudes differ because of their different viewing geometries. The maximum observed LOS displacement was approximately +4 cm in the ascending geometry and −3.0 cm in the descending geometry. LOS displacement is defined as positive towards the satellite and negative away from it. The opposite signs indicate different projections of the displacement vector onto the two radar viewing directions and do not, by themselves, uniquely determine the east–west and vertical components.

These components were estimated using the LOS observation equations, incorporating the incidence angle and satellite heading of each track. Because two viewing geometries cannot independently resolve all three displacement components, the north–south component was assumed negligible in the decomposition. Uncertainties in the derived east–west and vertical displacements were assessed through propagation of the LOS measurement uncertainties using the covariance matrix of the inversion. The resulting components should therefore be interpreted in light of this assumption and the uncertainty associated with each viewing geometry.

LOS profiles were extracted for both geometries, including profiles crossing the epicentral area and profiles extending toward the nearest mapped fault, to characterize the deformation gradients and spatial variation. The complementary ascending and descending observations were subsequently integrated to resolve the principal E–W and vertical components of the observed co-seismic deformation.



(a) **(b)**

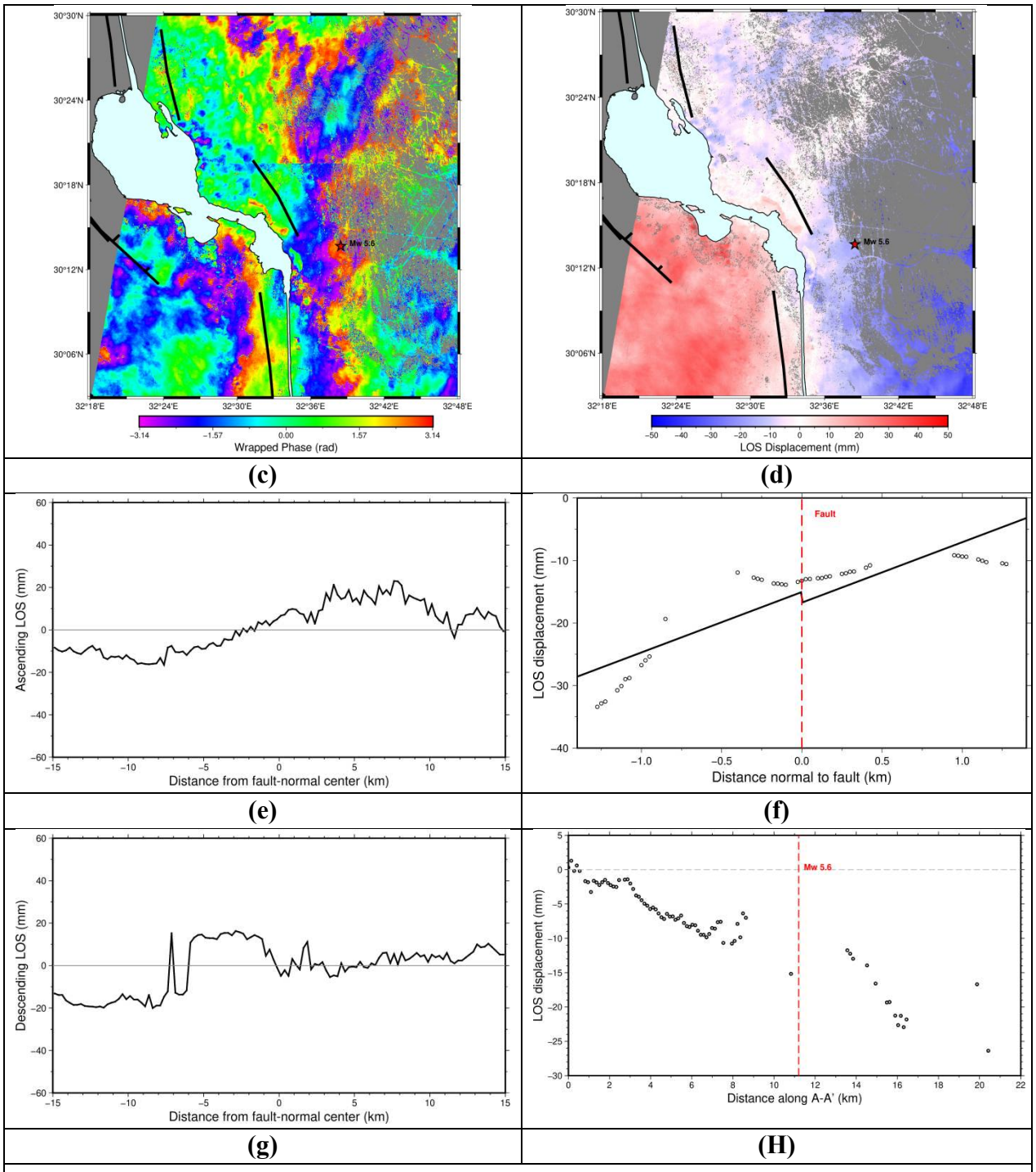


Fig.12: Ascending–descending comparison of the co-seismic deformation: (a) ascending filtered phase, (b) ascending LOS displacement, (c) descending filtered phase, (d) descending LOS displacement, (e) ascending LOS profile, (f) ascending LOS gradient profile, (g) descending LOS profile, and (h) descending LOS gradient profile.

4.5 E-W and Vertical Deformations

Combining the ascending and descending LOS observations yields the E–W and vertical displacement components (Fig. 13). The E–W component reaches approximately −.257 cm, indicating westward motion, whereas the vertical component reaches approximately +3.05 cm. The vertical displacement pattern shows uplift east of the Suez Canal and subsidence west of it (Fig. 13b). Although this distribution indicates a predominantly vertical deformation pattern, its polarity is not straightforwardly consistent with the expected surface response of a simple NE-dipping normal fault with a strike of 326°. This apparent discrepancy may reflect the contribution of three-dimensional fault geometry, distributed deformation, or uncertainties associated with the LOS decomposition and the different acquisition intervals. Because the ascending and descending pairs span slightly different periods (22 July–3 August and 24 July–5 August, respectively), the decomposition also assumes negligible deformation between 3 and 5 August. Therefore, the retrieved vertical pattern should be interpreted cautiously and should not be considered, by itself, as definitive evidence for the sense of slip on the proposed fault plane.

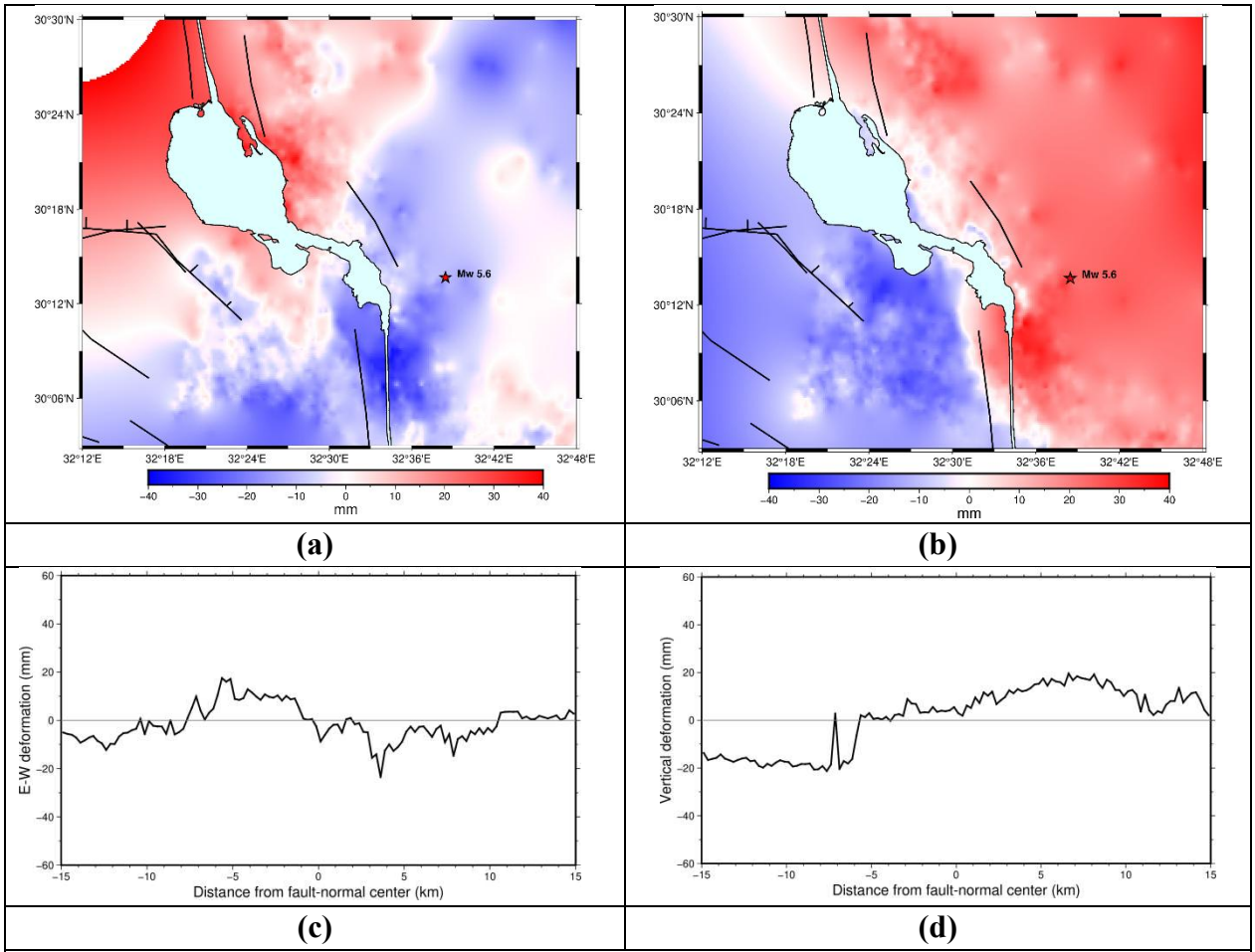


Fig.13: Resolved co-seismic deformation components derived from ascending and descending LOS observations: (a) E–W deformation, (b) vertical deformation, (c) E–W profile, and (d) vertical deformation profile.

4.6 Seismicity-Based Fault Geometry and Slip Model

The source geometry of the Mw 5.6 earthquake on 3 August 2026 was constrained using the three-dimensional hypocentral distribution and focal mechanism. Seismicity is concentrated around the main shock (Fig. 14a), while The rose diagram of the mapped structural segments shows dominant WNW–ESE and NNW–SSE trends, with no clear NE–SW dominance (Fig. 14b). The coseismic slip distribution was estimated by inverting the ascending and descending Sentinel-1 LOS observations using an elastic half-space dislocation model, with the fault surface discretized into subfaults and spatial smoothing applied to stabilize the inversion. The modeled slip is concentrated near the main shock hypocenter, reaching a maximum of ~13.6 cm at ~5 km depth near 30.33°N, 32.66°E. The slip model was restricted to a localized source area consistent with the Mw 5.6 earthquake. Model performance was evaluated by comparing observed and modeled LOS displacements. Residual maps, RMS misfit, variance reduction, and resolution tests are needed to further assess the model fit and the reliability of the inferred slip distribution.

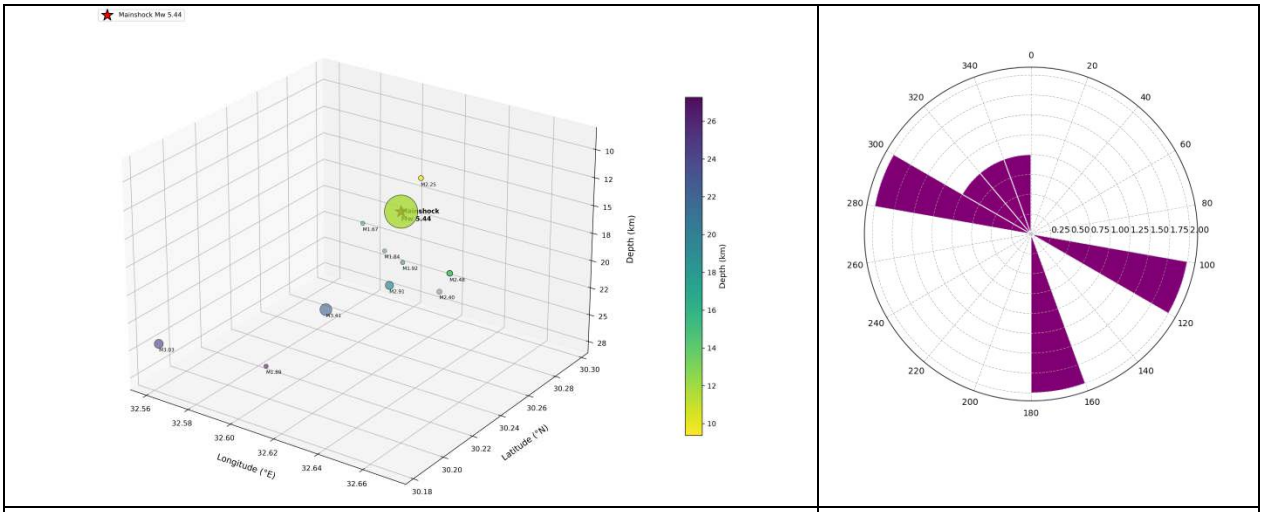


Fig.14: Seismicity distribution and fault-slip model of the 3 August 2026 Mw 5.6 Suez earthquake. (a) 3D distribution of earthquake hypocenters with latitude, longitude, and depth. (b) Rose diagram showing the dominant orientations of mapped faults surrounding the earthquake source, with prevailing WNW–ESE and NNW–SSE trends. (c) Fault-slip model. Yellow circles indicate pre-shock locations, cyan circles indicate after-shock locations, and the red star indicates the epicenter of the 2026 Suez earthquake.

4.7 Bouguer Gravity Anomaly and Correction Workflow

The Bouguer gravity anomaly served as the primary regional gravity dataset utilized for further structural assessment. The Bouguer gravity anomaly was derived from the satellite-only GOCO2025s gravity field, truncated at spherical harmonic degree and order 300, after removing GRS80 normal gravity and applying topographic and bathymetric corrections based on ETOPO1 using the tesseroid method. The resulting grid was transformed to a local metric coordinate system. Grid extension and cosine tapering were applied before frequency-domain processing to minimize edge effects and spectral leakage. The Bouguer anomaly (Fig. 15) reveals a broad positive domain in the west and a relatively negative domain in the east, separated by a pronounced gravity transition between approximately 31.5° and 32.7°E. This transition may reflect lateral density variations associated with sediment thickness, basement configuration, lithology, and deeper crustal structure. The earthquake's epicenter is located near this transition, implying that the source region is defined by substantial subsurface diversity. Its structural significance was further examined using the Moho contribution, residual gravity field, gravity derivatives, and published fault data.

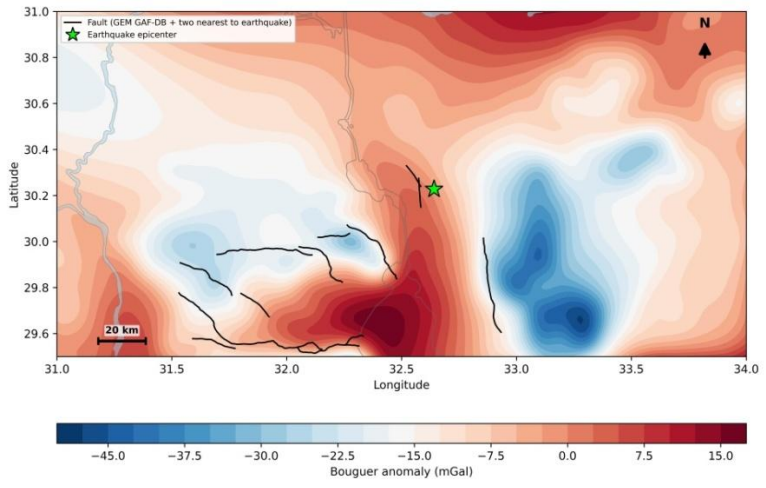


Fig.15: Bouguer gravity anomaly together with the earthquake epicenter, well locations, and published fault traces. The map provides the regional gravity framework for the subsequent structural analyses.

4.7.1 Moho Correction and Residual Gravity

The regional Moho model used in the analysis is shown in (Fig. 16) (after Sayed et al., 2025), and its gravitational effect was forward-modeled assuming a crust–mantle density contrast of 0.40 g cm^{-3}, the calculated Moho effect and residual gravity field are presented in (Fig. 17a). The correction indicates that part of the broad gravity variation, particularly the eastern gravity low, is related to crustal-thickness variations. After removing the Moho contribution, the pronounced local gravity gradients around the epicenter remain, including a positive residual anomaly to the south bounded by negative anomalies to the west and east (Fig. 17b). Their persistence suggests that these features are mainly associated with shallower crustal density contrasts rather than long-wavelength Moho variations. Given the earthquake focal depth of approximately 11.69 km below sea level, well above the modeled Moho, the Moho geometry is interpreted as a regional tectonic framework rather than a direct representation of the earthquake rupture.

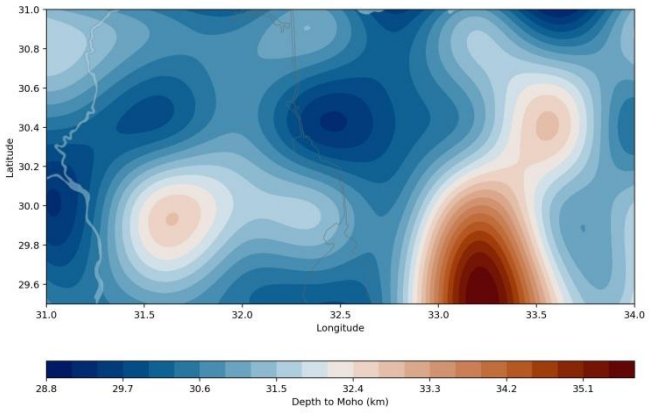
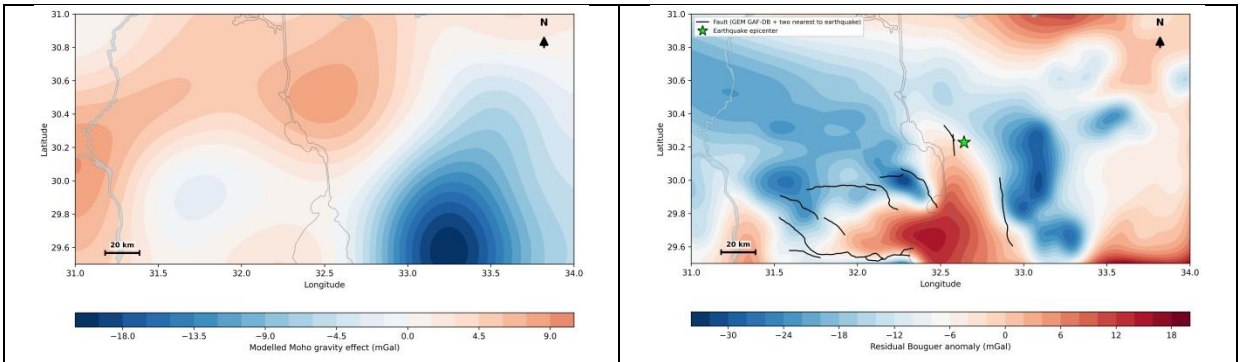


Fig.16: Regional depth-to-Moho model used in the analysis (after Sayed et al., 2025).



(a) **(b)**

Fig.17: (a) Calculated gravitational effect of the Moho and **(b)** residual Bouguer gravity anomaly after removal of the Moho contribution.

4.7.2 Euler Deconvolution Solutions

The Euler deconvolution results vary with the selected structural index (SI). The structural index was selected based on the assumed source geometry rather than solution clustering alone. SI = 0 yielded depths of 6–8 km, consistent with a fault-related density boundary, whereas the greater clustering of SI = 1 solutions near the epicentre does not necessarily indicate a more appropriate source geometry. Within a 10-km radius, 25 accepted SI = 1 solutions were identified, with a median estimated depth of 14.8 km and an interquartile range of 13.6–18.4 km (Fig. 18). The SI = 0 solutions were fewer and generally concentrated at depths of approximately 6–8 km, whereas SI = 2 solutions occurred mainly at 20–25 km depth. The SI = 1 population therefore defines a principal gravity-source depth range of approximately 15 km in the vicinity of the earthquake (Fig. 18).

4.7.3 Gravity-Derived Structural Orientation

The orientation of the dominant gravity-defined structure near the earthquake epicenter was estimated using a horizontal-gravity-gradient (HGG)-weighted structure-tensor analysis within a radius of 12 km from the epicenter, so that locations characterized by stronger lateral gravity gradients exerted greater influence on the estimated orientation. The resulting dominant structural trend is approximately N22°W–S22°E, corresponding to bearings of 338°/158°. This orientation is consistent with the broader NNW–SSE to NW–SE structural grain of the Gulf of Suez (Fig. 19).

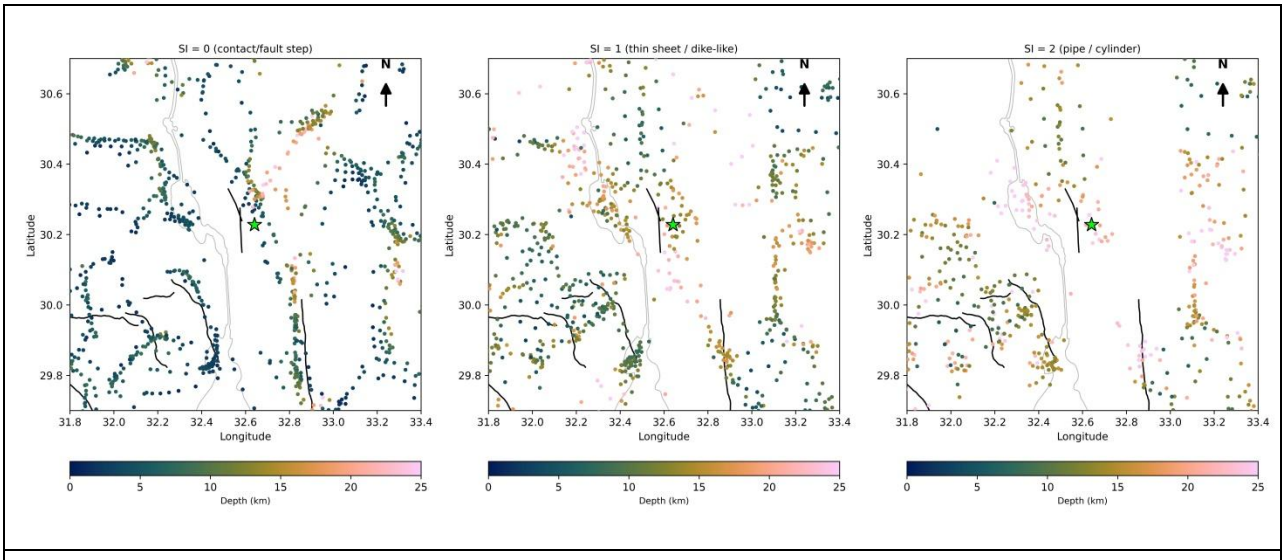
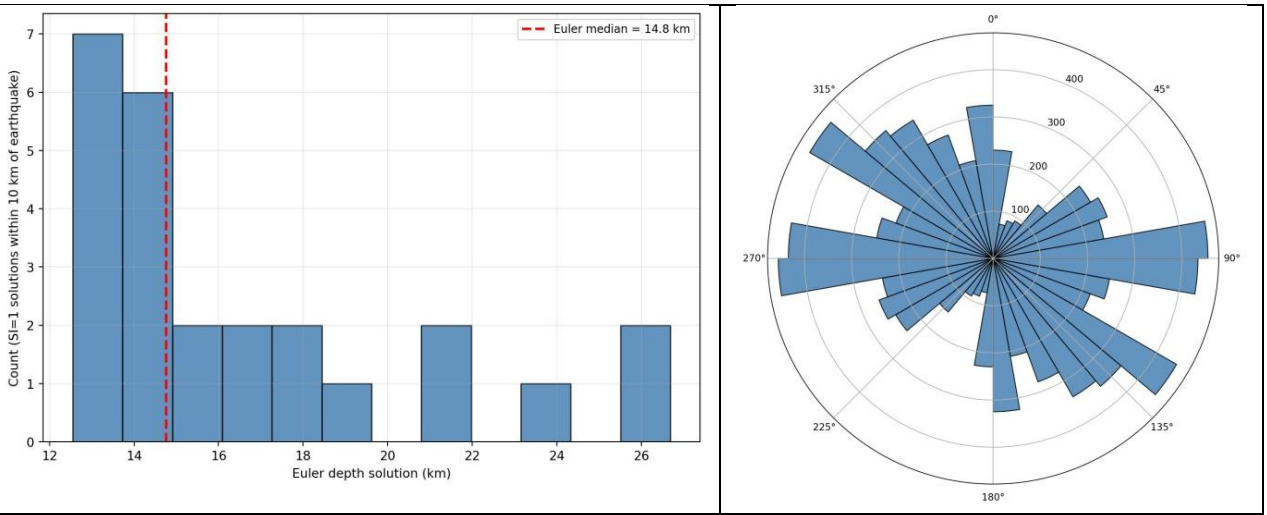


Fig.18: Euler deconvolution solutions for SI = 0, 1, and 2, color-coded by depth.



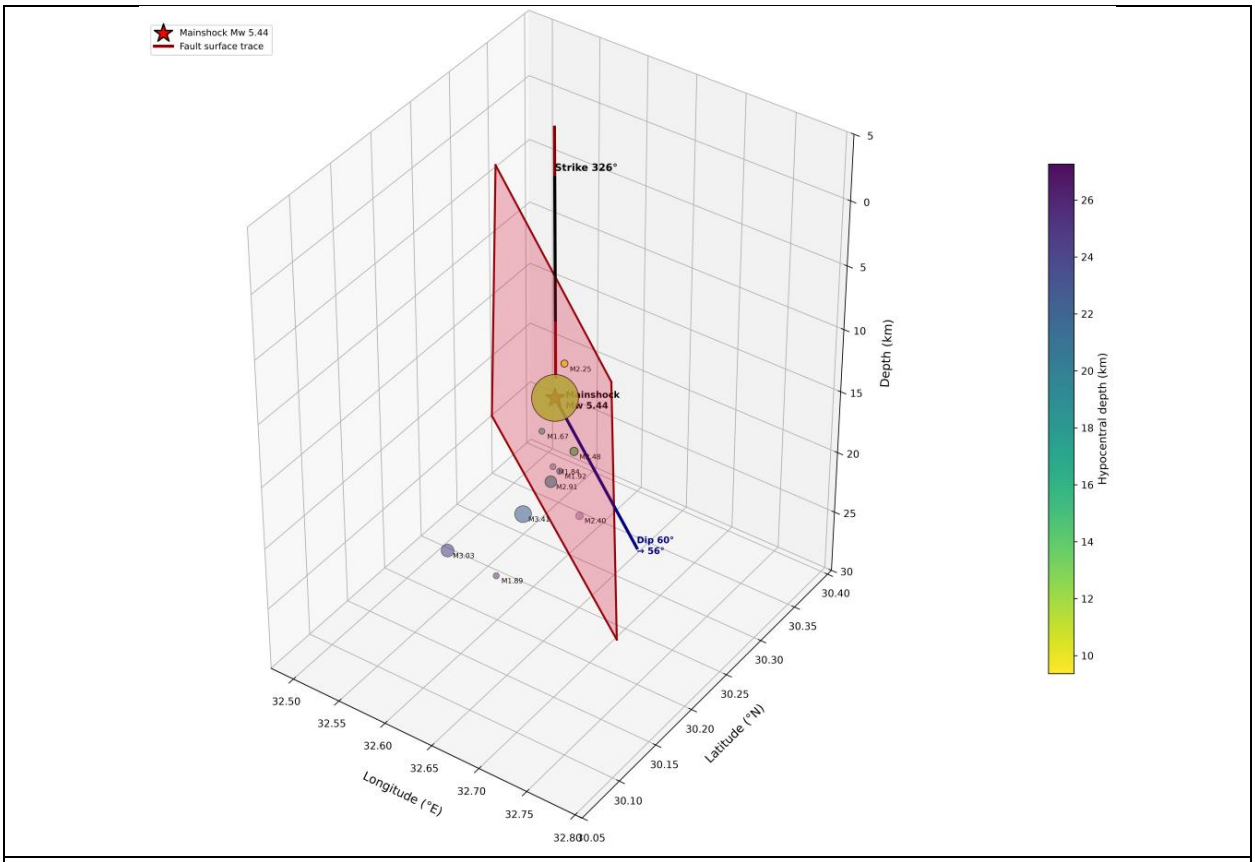
a) **b)**

Fig.19: a) Histogram of SI = 1 Euler depth solutions within 10 km of the earthquake epicenter. Median depth (dashed red line) = 14.8 km, b) Fault-trend rose diagram showing the principal structural orientations identified from the fault compilation used in this study.

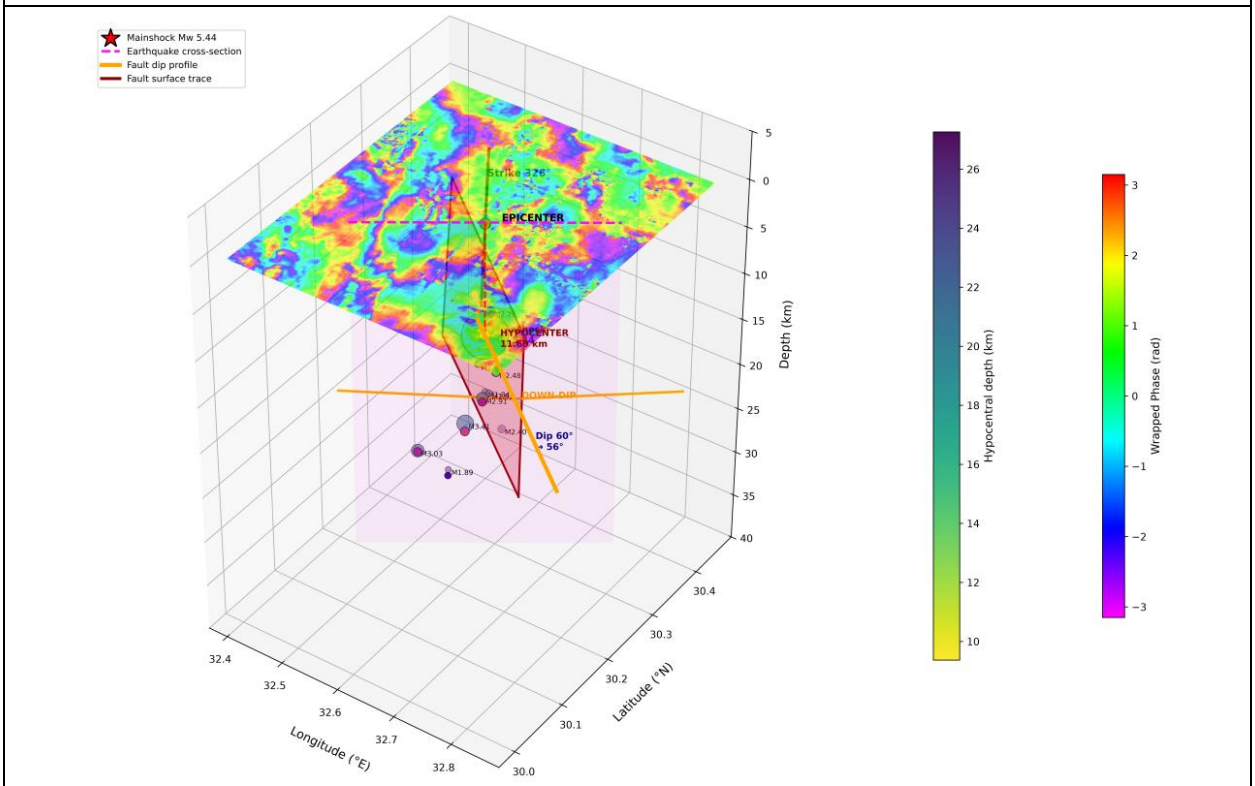
4.8 Integrated Seismic–InSAR Fault Model

An integrated fault model was developed by combining Hypocentres, aftershock distribution, the focal-mechanism solution, and Sentinel-1 observations. The main shock is located at ~11.69 km depth, with aftershocks extending to ~27 km. The inferred fault strikes approximately 326°, consistent with the NW–SE structural trend and the 326° strike of the focal-mechanism nodal plane (dip 55°). The observed vertical deformation, characterized by subsidence west of the epicenter and uplift to the east, favors a SW-dipping geometry and is consistent with 35° and 55° nodal plane. The interferometric phase and LOS displacement were superimposed on the preferred fault geometry (Fig. 20), and transverse and longitudinal profiles show maximum LOS deformation of ~2.2 cm near the epicentral area. Deformation is concentrated near the up-dip portion of the inferred plane, whereas deeper aftershocks extend beyond the main deformation zone. The preferred geometry is therefore interpreted as a SW-dipping normal fault, while the broader 326°–338° structural trend reflects the regional rift-related fault framework.

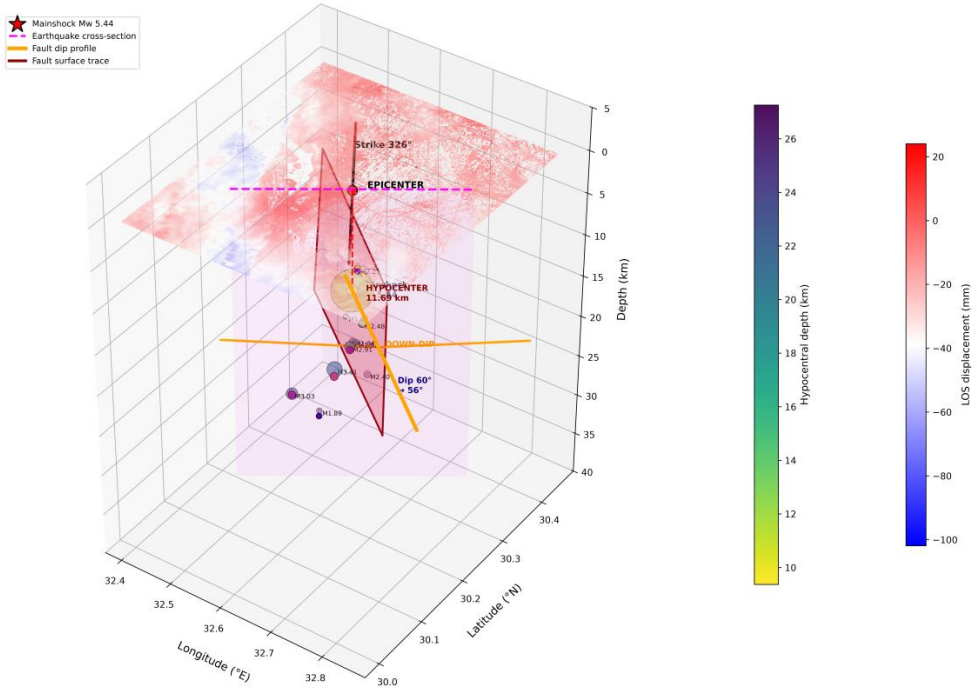
The LOS displacement was projected along the dip direction of the inferred fault plane (Fig. 21). The original LOS profile shows a broad, near-linear variation from approximately −30 to +35 mm over the 50-km profile, with a localized perturbation near the projected fault trace. Because such a long-wavelength linear trend may reflect orbital or atmospheric effects, a planar ramp was removed before interpreting the localized deformation associated with the fault. The projected fault geometry is illustrative only. The ~17.6 km depth is inferred from the assumed dip and profile geometry, rather than independently constrained. The main shock hypocentral depth of ~11.7 km provides the principal depth constraint on the earthquake source.


Mainshock Mw 5.44
Fault surface trace
Strike 326°
Dip 60°
→ 56°
M2.25
M1.67
M2.48
M2.91
M3.41
M2.40
M3.03
M1.89
Depth (km)
Longitude (°E)
Latitude (°N)
Hypocentral depth (km)

(a)


Mainshock Mw 5.44
Earthquake cross-section
Fault dip profile
Fault surface trace
Strike 326°
EPICENTER
HYPOCENTER
11.56 km
DOWN-DIP
Dip 60°
→ 56°
Depth (km)
Longitude (°E)
Latitude (°N)
Hypocentral depth (km)
Wrapped Phase (rad)

(b)



(c)

Fig.20: Integrated three-dimensional fault model of the 3 August 2026 Mw 5.6 Suez earthquake sequence. (a) Three-dimensional distribution of the main shock and aftershocks with the inferred fault plane, showing the hypocentral depth and fault geometry. (b) Interferometric phase field superimposed on the inferred earthquake source geometry. (c) LOS displacement field and transverse/longitudinal profiles across the inferred fault plane, illustrating the spatial distribution and magnitude of the observed deformation.

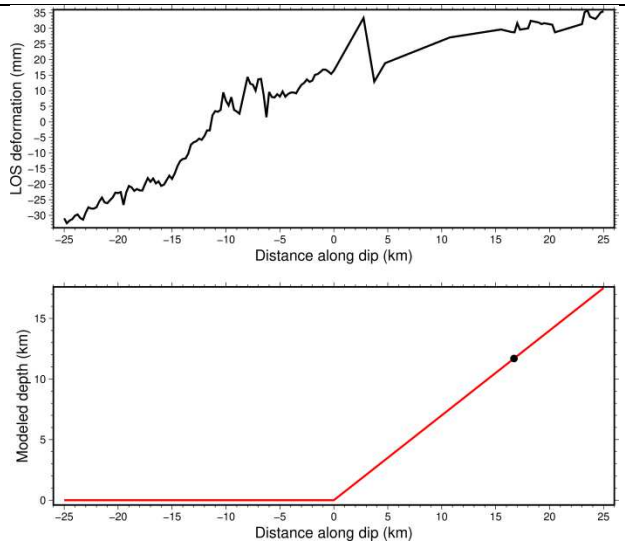


Fig.21: Relationship between LOS displacement, distance along the modeled fault dip, and depth of the inferred fault plane. The profile illustrates the variation of LOS deformation along the fault dip and the modeled subsurface extent of the earthquake source, reaching approximately 17.6 km depth.

5. Discussion

5.1 Reliability and Nature of the Observed Deformation

The InSAR observations reveal deformation around the epicentral region in both ascending and descending geometries. However, the principal LOS sign change occurs near the Suez Canal and Great Bitter Lake, where decorrelation may cause unwrapping discontinuities between coherent areas. Consequently, the broad uplift–subsidence pattern should be interpreted cautiously, and the approximately 7 mm fault-localized LOS step requires further validation before being attributed to tectonic displacement. The available observations are therefore insufficient to establish the fault dip direction conclusively. The SW-dipping normal-fault geometry remains a possible interpretation, but the apparent subsidence west of the epicentre and uplift to the east cannot independently establish this configuration because the pattern may be affected by unwrapping errors. Joint inversion of the ascending and descending InSAR data provides a test of the deformation fit under the assumed fault geometry, but it is not an independent validation of the dip direction because the same observations were used to assess the source model. Independent confirmation would require additional evidence, such as coherent unwrapping paths across the affected area, consistent displacement patterns away from the decorrelated zone, or independent geodetic observations. The LiCSBAS time series from 1 May to 31 July 2026 shows only weak fluctuations without a persistent spatial or temporal trend. These observations do not provide convincing evidence of detectable pre-seismic deformation. This integrated interpretation is consistent with a SW-dipping plane as the preferred source geometry.

5.2 Relationship between deformation and seismicity

The main shock hypocenter lies at ~11.69 km depth, whereas the aftershock sequence extends to ~27 km, indicating that seismic activity occupies a broader depth range than the zone of principal surface deformation. The concentration of the strongest LOS deformation near the epicenter, together with the alignment of seismicity along the inferred NW–SE plane (Figs. 14 and 20), supports a link between the surface deformation and the activated structure. The deeper aftershocks are unlikely to produce resolvable surface deformation and may represent post-main shock adjustment within the broader seismogenic volume. The modeled slip concentration at ~5 km depth is shallower than the hypocenter, consistent with up-dip rupture propagation, but its reliability depends on the inversion approach.

5.3 Gravity Constraints on the Earthquake Source

Gravity data provide regional constraints on subsurface structure near the earthquake source. The dominant gravity-derived orientation of 338°/158° is broadly consistent with the modeled fault strike of 326°, although the 12° difference and the limited spatial resolution of approximately 65 km warrant cautious interpretation. Similarly, the median Euler depth of 14.8 km differs from the earthquake focal depth of 11.69 km and the modeled slip depth of approximately 5 km. These relationships are consistent with a possible structural association but do not independently

demonstrate structural control. Such an interpretation would be weakened if higher-resolution data revealed no spatial correspondence between gravity-derived boundaries and the source region, or if independent structural observations showed incompatible fault orientations and locations.

5.4 Tectonic Significance

The main shock occurred near the northern termination of the Suez Rift, where NW–SE to NNW–SSE rift-related structures interacts with inherited E–W to WNW–ESE structures of the Cairo–Suez district. The normal-faulting mechanism, the NW–SE orientation of the deformation field, and the gravity-derived trend of 338°/158° suggest that the earthquake was accommodated by a pre-existing rift-related structure. The preferred SW-dipping geometry is consistent with the observed pattern of westward subsidence and eastward uplift. The event indicates that moderate earthquakes capable of producing measurable surface deformation can occur within this structurally complex transition zone, highlighting the importance of individual fault characterization for seismic-hazard assessment in the Cairo–Suez region.

5.5 Integrated Interpretation and Study Limitations

The combined InSAR, seismicity, focal-mechanism, fault-geometry, and gravity results provide a coherent interpretation of the 3 August 2026 Mw 5.6 Suez earthquake. InSAR constrains the spatial pattern of surface deformation, while the seismicity and focal mechanism define the source location and normal-faulting style. Their integration indicates that the strongest deformation is concentrated near the shallow part of the inferred fault, whereas the deeper aftershocks occupy a broader seismogenic volume. Gravity data independently support the presence of subsurface structural contrasts near the epicentral area, with Euler deconvolution and structural analysis indicating orientations consistent with the regional rift framework.

The integrated results suggest that the earthquake occurred along a pre-existing and structurally heterogeneous fault system associated with the northern Gulf of Suez. The three-month LiCSBAS analysis from 1 May to 31 July 2026 revealed only low-amplitude displacement variations without a systematic temporal or spatial trend. These signals cannot be confidently attributed to tectonic deformation and are therefore not considered evidence of a confirmed earthquake precursor. Several limitations should be considered. These include residual atmospheric and orbital effects in the InSAR data, uncertainties associated with phase unwrapping near water bodies, limited constraints on the focal-mechanism solution from first-motion polarities, and uncertainties in the inferred fault geometry and slip distribution. In addition, the satellite-derived gravity data provide regional rather than high-resolution constraints on shallow structures. Future studies should incorporate atmospherically corrected multi-temporal InSAR, joint geodetic–seismological inversion, and independent GNSS and terrestrial gravity observations to further refine the source geometry and deformation field.

6. Conclusions

We investigated the deformation and structural setting of the 3 August 2026 Mw 5.6 Suez earthquake using Sentinel-1 InSAR, seismicity, focal-mechanism information, and satellite gravity data. The main conclusions are:

- **Co-seismic deformation:** Ascending and descending Sentinel-1 interferograms reveal coherent deformation around the epicenter, with maximum LOS values of ~4cm and ~3 cm, respectively. A localized LOS step of ~7 mm occurs across the nearest mapped fault, while the resolved E–W and vertical components reach approximately 2.5 and 3.05 cm.

- **Pre-event deformation:** The three-month LiCSBAS analysis from 1 May to 31 July 2026 shows only low-amplitude variations without a systematic spatial or temporal pattern. No convincing evidence of pre-seismic deformation was identified.

- **Seismicity and source mechanism:** The earthquake sequences and focal mechanism point to primarily normal faulting related with the NW-SE regional structural grain, while the first-motion solution is very poorly restricted.

- **Fault geometry and slip:** Integration of seismicity and InSAR favours a fault striking approximately 326° with a SW-dipping geometry consistent with the 152°/50° nodal plane. The modeled maximum slip is ~13.6 cm at ~5 km depth near the main shock source region.

- **Gravity constraints:** The epicenter lies near a pronounced density boundary. Euler solutions yield a median source-related depth of ~14.8 km, while the dominant gravity-derived trend (338°/158°) is consistent with the regional NNW–SSE to NW–SE rift-related structural grain.

- **Tectonic significance:** The earthquake occurred on a pre-existing rift-related structure near the northern termination of the Suez Rift. This structurally complex transition zone is essential to seismic-hazard assessment in the Cairo–Suez area because the integrated seismic, InSAR, and gravity studies show that it is still capable of producing moderate and high earthquakes.

Acknowledgments

The authors gratefully acknowledge the National Research Institute of Astronomy and Geophysics (NRIAG) and the Egyptian National Seismological Network (ENSN) for providing earthquake catalogue data and scientific support. We acknowledge the European Space Agency (ESA) Copernicus Sentinel-1 mission for the SAR data (Contains modified Copernicus Sentinel data (2026) and the Alaska Satellite Facility (ASF) for data access. We also thank the COMET LiCSAR and LiCSBAS teams for providing InSAR processing products and time-series analysis

tools, and the developers of GMTSAR and SNAPHU for the software used in SAR processing and phase unwrapping. Satellite gravity data were obtained from the International Centre for Global Earth Models (ICGEM), including the GOCO2025s model. We further acknowledge the providers of the SRTM digital elevation model through the United States Geological Survey (USGS) and the ETOPO1 topography–bathymetry dataset. These data and tools supported the analysis of co-seismic deformation, seismicity, and the regional structural setting of the 3 August 2026 Mw 5.6 Suez earthquake.

Author contributions

M.S.E. (Mahmoud S. Etman) contributed to Sentinel-1 InSAR data processing, co-seismic deformation analysis, and interpretation of the resulting deformation patterns. G.Q. (Gad Qady) contributed to the geological and structural characterization of the study area, seismicity interpretation, and integration of the geological and geophysical datasets.) H.S. (Hussein Sabry) contributed to seismicity analysis, focal-mechanism interpretation, and assessment of the earthquake source characteristics. M.S. (Motaaz Sayed) contributed to satellite gravity data processing, gravity anomaly analysis, and subsurface structural interpretation. A.H. (Ahmed Hamed) contributed to distribution of seismicity analysis and depth estimation of fault geometry. M.S.M. (Mohamed S. Mahrous) contributed to data integration, structural interpretation and preparation of the final maps and figures. All authors contributed to the conceptualization and design of the study, interpretation of the integrated results, manuscript preparation, review and editing, and approved the final version of the manuscript.

Data availability

Data sets generated during the current study are available from the first author on reasonable request.

Competing Interests

The authors declare no competing interests.

Funding

This research has received no funding.

References

Abdelazim, M., Samir, A., El-Nader, I. A., Badawy, A., & Hussein, H. (2016). Seismicity and focal mechanisms of earthquakes in Egypt from 2004 to 2011. NRIAG Journal of Astronomy and Geophysics, 5(2), 393-402. https://doi.org/10.1016/j.nrjag.2016.08.002.

Alsharhan, A. S. (2003). Petroleum geology and potential hydrocarbon plays in the Gulf of Suez rift basin, Egypt. *AAPG Bulletin, 87*(1), 143–180. https://doi.org/10.1306/062002870143

Bosworth, W., Huchon, P., & McClay, K. (2005). The Red Sea and Gulf of Aden basins. *Journal of African Earth Sciences, 43*(1–3), 334–378. https://doi.org/10.1016/j.jafrearsci.2005.07.020.

Bürgmann, R., Hilley, G., Ferretti, A., & Novali, F. (2006). Resolving vertical tectonics in the San Francisco Bay area from permanent scatterer InSAR and GPS analysis. *Geology, 34*(3), 221–224. https://doi.org/10.1130/G22064.1.

Bosworth, W., & Taviani, M. (1996). Late Quaternary reorientation of stress field and extension direction in the southern Gulf of Suez, Egypt: Evidence from uplifted coral terraces, mesoscopic fault arrays, and borehole breakouts. *Tectonics, 15*(4), 791–802. https://doi.org/10.1029/95TC03851.

Bosworth, W., Taviani, M., & Rasul, N. M. A. (2019). Neotectonics of the Red Sea, Gulf of Suez and Gulf of Aqaba. In N. M. A. Rasul & I. C. F. Stewart (Eds.), *Geological setting, palaeoenvironment and archaeology of the Red Sea* (pp. 11–35). Springer. https://doi.org/10.1007/978-3-319-99408-6_2.

Colletta, B., Le Quellec, P., Letouzey, J., & Moretti, I. (1988). Longitudinal evolution of the Suez rift structure (Egypt). *Tectonophysics, 153*(1–4), 221–233. https://doi.org/10.1016/0040-1951(88)90017-0.

El Khrepy, S., Koulakov, I., & Al-Arifi, N. (2016). Crustal and uppermost mantle structure beneath the continental rifting area of the Gulf of Suez from earthquake tomography. *Tectonophysics, 668–669*, 92–104. https://doi.org/10.1016/j.tecto.2015.11.027.

Etman, M. S., Mohamed, A. S., Ayyad, H. M., & Abu-Bakr, M. M. (2022). Monitoring the deformation of the western part of the Nile Delta, Egypt using sentinel-1A and seismicity data. The Iraqi Geological Journal, 27-38. https://doi.org/10.46717/igj.55.2D.3ms-2022-10-19.

Etman, M. S., Mohamed, S. A., Saleh, S., Mohamed, A. M. S., & Fergawy, K. O. (2025). Analyzing recent deformation in Wadi Hagul, Eastern Desert, Egypt, via advanced remote sensing and geodetic data processing. *Journal of Applied Geodesy*, *19*(1), 59-73. https://doi.org/10.1515/jag-2024-0039.

Etman, M. S., Mohamed, A. M. S., Saleh, S., Mohamed, S. A., & Fergawy, K. O. (2025). Geological Structures Assessment in Wadi Hagul, Northwestern Gulf of Suez, Egypt, Using Gravity and Magnetic Techniques. *Jordan Journal of Earth & Environmental Sciences*, *16*(2), 163.

Farag, T., Sobh, M., & Mizunaga, H. (2022). 3D constrained gravity inversion to model Moho geometry and stagnant slabs of the Northwestern Pacific plate at the Japan Islands. *Tectonophysics*, *829*, 229297. https://doi.org/10.1016/j.tecto.2022.229297.

Fernandez-Blanco, D., de Gelder, G., & Aiden-Lee Jackson, C. (2025). Is the Suez Rift in its post-rift phase? *Geophysical Research Letters, 52*(21), e2025GL117313. https://doi.org/10.1029/2025GL117313.

Gawthorpe, R. L., Jackson, C. A. L., Young, M. J., Sharp, I. R., Moustafa, A. R., & Leppard, C. W. (2003). Normal fault growth, displacement localisation and the evolution of normal fault populations: the Hammam Faraun fault block, Suez rift, Egypt. *Journal of*

Structural Geology, *25*(6), 883-895. https://doi.org/10.1016/S0191-8141(02)00088-3.
Guo, N., Wu, Y., & Zhang, Q. (2022). Coseismic and Pre-seismic Deformation Characteristics of the 2022 MS 6.9 Menyuan Earthquake, China *Pure and Applied Geophysics*, *179*(9), 3177-3190. https://doi.org/10.1007/s00024-022-03128-3.
Hanssen, R. F. (2001). *Radar interferometry: Data interpretation and error analysis*. Kluwer Academic Publishers. https://doi.org/10.1007/0-306-47633-9
Hinze, W. J. (2003). Bouguer reduction density, why 2.67. *Geophysics*, *68*(5), 1559-1560. https://doi.org/10.1190/1.1620629.
Hooper, A., Bekaert, D., Spaans, K., & Arıkan, M. (2012). Recent advances in SAR interferometry time series analysis for measuring crustal deformation. *Tectonophysics, 514–517*, 1–13. https://doi.org/10.1016/j.tecto.2011.10.013
Hussein, H. M., Abou Elenean, K. M., Marzouk, I. A., Korrat, I. M., Abu El-Nader, I. F., Ghazala, H., & ElGabry, M. N. (2013). Present-day tectonic stress regime in Egypt and surrounding area based on inversion of earthquake focal mechanisms. *Journal of African Earth Sciences, 81*, 1–15. https://doi.org/10.1016/j.jafrearsci.2012.12.002
Hussein, H. M., Marzouk, I. A., Moustafa, A. R., & Hurukawa, N. (2006). Preliminary seismicity and focal mechanisms in the southern Gulf of Suez: August 1994 through December 1997. *Journal of African Earth Sciences, 45*(1), 48–60. https://doi.org/10.1016/j.jafrearsci.2006.01.006.
Ince, E. S., Barthelmes, F., Reißland, S., Elger, K., Förste, C., Flechtner, F., & Schuh, H. (2019). ICGEM – 15 years of successful collection and distribution of global gravitational models, associated services and future plans. *Earth System Science Data, 11*, 647–674. https://doi.org/10.5194/essd-11-647-2019
Jackson, C. A.-L., Gawthorpe, R. L., Leppard, C. W., & Sharp, I. R. (2006). Rift-initiation development of normal fault blocks: Insights from the Hammam Faraun fault block, Suez Rift, Egypt. *Journal of the Geological Society, 163*(1), 165–183. https://doi.org/10.1144/0016-764904-164
Luo, H., Wang, T., Wei, S., Liao, M., & Gong, J. (2021). Deriving centimeter-level coseismic deformation and fault geometries of small-to-moderate earthquakes from time-series Sentinel-1 SAR images. *Frontiers in Earth Science, 9*, 636398. https://doi.org/10.3389/feart.2021.636398
Mahmoud, S., Reilinger, R., McClusky, S., Vernant, P., & Tealeb, A. (2005). GPS evidence for northward motion of the Sinai Block: Implications for E. Mediterranean tectonics. *Earth and Planetary Science Letters, 238*(1–2), 217–224. https://doi.org/10.1016/j.epsl.2005.06.063
Merryman Boncori, J. P. (2019). Measuring coseismic deformation with space borne synthetic aperture radar: A review. *Frontiers in Earth Science, 7*, 16. https://doi.org/10.3389/feart.2019.00016.
Morishita, Y., Kobayashi, T., Yarai, H. (2021). Nationwide urban ground deformation monitoring in Japan using Sentinel-1 LiCSAR products and LiCSBAS. *Progress in Earth and Planetary Science, 8*, 6. https://doi.org/10.1186/s40645-020-00402-7.
Moritz, H. (1980). *Geodetic reference system 1980*. International Association of Geodesy.

Morsy, M., Hussein, H. M., Abou Elenean, K. M., & El-Hady Elnashar, S. (2011). Stress field in the central and northern parts of the Gulf of Suez area, Egypt from earthquake fault plane solutions. *Journal of African Earth Sciences, 60*(5), 293–302. https://doi.org/10.1016/j.jafrearsci.2011.03.006

Moustafa, A. R., & Abd-Allah, A. M. (1992). Transfer zones with en echelon faulting at the northern end of the Suez Rift. *Tectonics, 11*(3), 499–506. https://doi.org/10.1029/91TC03184.

Öhlinger, F., Mayer-Gürr, T., Krauss, S., Dumitraschkewitz, P., Strasser, A., Süsser-Rechberger, B., Brockmann, J.M. and Niedermaier, J., (2026). The satellite-only gravity field model GOCO2025s. *Earth System Science Data Discussions*, *2026*, pp.1-27. https://doi.org/10.5194/essd-2026-639.

Okada, Y. (1985). Surface deformation due to shear and tensile faults in a half-space. *Bull. Seismol. Soc. Am*, *75*(4), 1135-1154.

Riguzzi, F., Pietrantonio, G., Piersanti, A., & Mahmoud, S. M. (2006). Current motion and short-term deformations in the Suez–Sinai area from GPS observations. *Journal of Geodynamics, 41*(5), 485–499. https://doi.org/10.1016/j.jog.2006.01.006.

Salamon, A., Hofstetter, A., Garfunkel, Z., & Ron, H. (2003). Seismotectonics of the Sinai subplate – The eastern Mediterranean region. *Geophysical Journal International, 155*(1), 149–173. https://doi.org/10.1046/j.1365-246X.2003.02017.

Sandwell, D., Mellors, R., Tong, X., Wei, M., & Wessel, P. (2011). Open radar interferometry software for mapping surface deformation. *Eos, Transactions American Geophysical Union, 92*(28), 234. https://doi.org/10.1029/2011EO280002.

Sayed, M., Sobh, M., Saleh, S., Othman, A., & Elmahmoudi, A. (2025). 3D crustal density modeling of Egypt using GOCE satellite gravity data and seismic integration. *Earthquake Science, 38*(2), 110–125. https://doi.org/10.1016/j.eqs.2024.09.003.

Steckler, M. S., Berthelot, F., Lyberis, N., & Le Pichon, X. (1988). Subsidence in the Gulf of Suez: implications for rifting and plate kinematics. *Tectonophysics*, *153*(1-4), 249-270. https://doi.org/10.1016/0040-1951(88)90019-4.

Styron, R., & Pagani, M. (2020). GEM global active faults database. *Earthquake Spectra*, *36*(1_suppl), 160-180. https://doi.org/10.1177/8755293020944182.

Uieda, L., Barbosa, V. C. F., & Braitenberg, C. (2016). Tesseroid: Forward-modeling gravitational fields in spherical coordinates. *Geophysics, 81*(5), F41–F48. https://doi.org/10.1190/geo2015-0204.1.

Yu, C., Li, Z., Penna, N. T., & Crippa, P. (2018). Generic atmospheric correction model for interferometric synthetic aperture radar observations. *Journal of Geophysical Research: Solid Earth*, *123*(10), 9202-9222.

Zhu, J., Zhang, B., Yao, S., & Cai, Y. (2025). Coseismic deformation, fault slip distribution, and stress changes of the 2025 MS 6.8 Dingri earthquake from Sentinel-1A InSAR observations. *Geosciences, 15*(11), 421. https://doi.org/10.3390/geosciences15110421